# Experimental and Theoretical Insights into the Electronic Properties of Anionic N-Heterocyclic Dicarbenes through the Rational Synthesis of Their Transition Metal Complexes

Alina A. Grineva,[†,‡] Oleg A. Filippov,[§,ǁ] Yves Canac,[†] Jean-Baptiste Sortais,[†,ǂ] Sergei E. Nefedov,[‡] Noël Lugan,[†,*] Vincent César[†,*] and Dmitry A. Valyaev[†,*]

*† LCC-CNRS, Université de Toulouse, CNRS, UPS, 205 route de Narbonne, 31077 Toulouse Cedex 4, France*

*‡ Kurnakov Institute of General and Inorganic Chemistry, Russian Academy of Sciences, 31 Leninsky Pr., Moscow, 119991, Russia*

*§ A. N. Nesmeyanov Institute of Organoelement Compounds (INEOS), Russian Academy of Sciences, 28 Vavilov str., GSP-1, B-334, Moscow, 119991, Russia*

ǁ *Shemyakin-Ovchinnikov Institute of Bioorganic Chemistry, Russian Academy of Sciences, 16/10 Miklukho-Maklay Str., Moscow 117997, Russia*

ǂ *Institut Universitaire de France, 1 rue Descartes, 75231 Paris Cedex 05, France*

# Supporting Information

# Table of Contents


**1. Copies of the NMR spectra for Mn(I) and Fe(II) NHC complexes** **S3**

Figures S1-S2. NMR spectra of complex $CpMn(CO)_2$(*μ-d*IMes)$Fe(CO)_2Cp$ (**3**) **S3-4**

Figures S3-S4. NMR spectra of complex [$CpFe(CO)_2$(*a*IMes)](OTf) ([**4**](OTf)) **S5-6**

Figures S5-S6. NMR spectra of complex [$CpFe(CO)_2$(*μ-d*IMes)$Fe(CO)_2Cp$](OTf) ([**5**](OTf)) **S7-8**

Figures S7-S8. NMR spectra of complex [$CpFe(CO)_2$(IMes)](OTf) ([**6**](OTf)) **S9-10**

**2. Electrochemical studies of Mn(I) and Fe(II) NHC complexes** **S11**

Figure S9. Cyclic voltammogram of complex $CpMn(CO)_2$(IMes) (**1**) **S11**

Figure S10. Cyclic voltammogram of complex $CpMn(CO)_2$(*μ-d*IMes)$Fe(CO)_2Cp$ (**3**) **S11**

Figure S11. Cyclic voltammogram of complex [$CpFe(CO)_2$(*a*IMes)](OTf) ([**4**](OTf)) **S12**

Figure S12. Cyclic voltammogram of complex [$CpFe(CO)_2$(*μ-d*IMes)$Fe(CO)_2Cp$](OTf) ([**5**](OTf)) **S12**

Figure S13. Cyclic voltammogram of complex [$CpFe(CO)_2$(IMes)](OTf) ([**6**](OTf)) **S13**

**3. Computational results** **S14**

Table S1. Key structural data of calculated Mn(I) and Fe(II) NHC complexes **S14**

Table S2. Energy difference between the conformers Mn(I) and Fe(II) NHC complexes **S14**

Table S3. Characteristics of bond critical points for $\pi$(C=C)...$\pi$*(CO) interligand interactions in optimized Mn(I) and Fe(II) NHC complexes **S14**

Figures S14-S18. AIM molecular graphs for Mn(I) and Fe(II) NHC complexes **S15**

Table S4. Characteristics of bond critical points for metal-carbene bonds in optimized Mn(I) and Fe(II) NHC complexes **S17**

Table S5. Selected AIM charges for optimized Mn(I) and Fe(II) NHC complexes **S17**

Table S6. Selected NBO charges for optimized Mn(I) and Fe(II) NHC complexes **S17**

Table S7. Calculated $\nu_{CO}$ bands for optimized Mn(I) and Fe(II) NHC complexes **S18**

Table S8. ETS-NOCV analysis data for metal-carbene bonding in optimized Mn(I) and Fe(II) NHC complexes bearing IMes, *a*IMes and *d*IMes ligands **S18**

Comparison of metal-carbon bonding between model σ-complexes $Cp(CO)_2Fe{-}R$ (**7-9**) and Fe(II) IMes, *a*IMes and *d*IMes complexes **S19**

Figure S19. DFT optimized geometries for Fe(II) complexes $Cp(CO)_2Fe{-}R$ (**7-9**) **S19**

Table S9. Comparison of the selected characteristics of BCPs for Fe−C bonds in Fe(II) σ-complexes **7-9** with those of Fe−NHC bonds in IMes, *a*IMes and *d*IMes complexes **S19**

Table S10. The comparison of ETS-NOCV data for Fe−C bonding in optimized Fe(II) σ-complexes **7-9** with those of Fe−NHC bonding in IMes, *a*IMes and *d*IMes complexes **S20**

Figures S20-S22. NOCV deformation electron density for model Fe(II) σ-complexes $Cp(CO)_2Fe{-}R$ **7-9** **S21**

Figure S23-S34. NOCV deformation electron density for Mn(I) and Fe(II) NHC complexes bearing IMes, *a*IMes and *d*IMes ligands **S23**

## 1. Copies of the NMR spectra for Mn(I) and Fe(II) NHC complexes

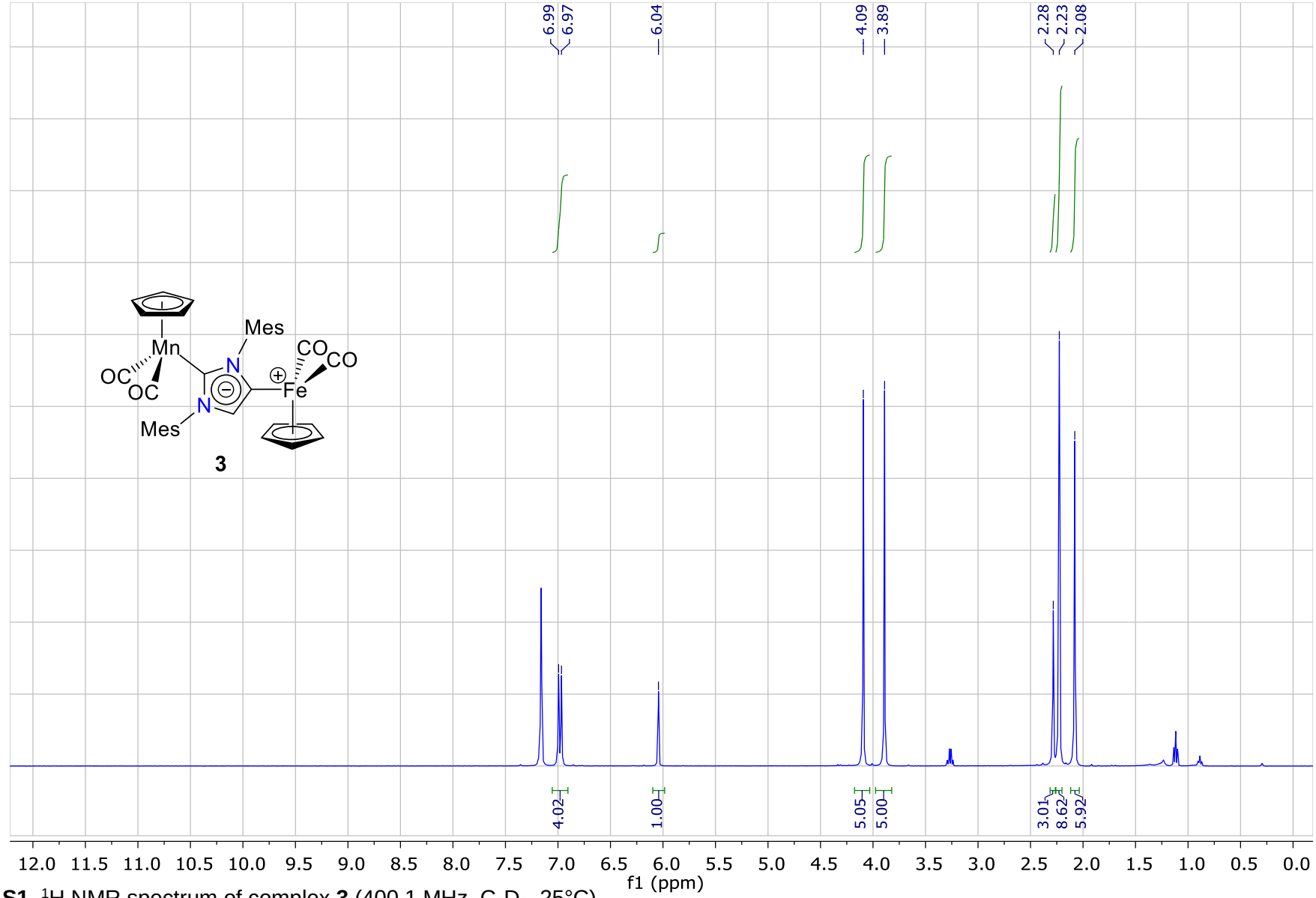


**Figure S1**. $^{1}$H NMR spectrum of complex **3** (400.1 MHz, $C_6D_6$, 25°C)

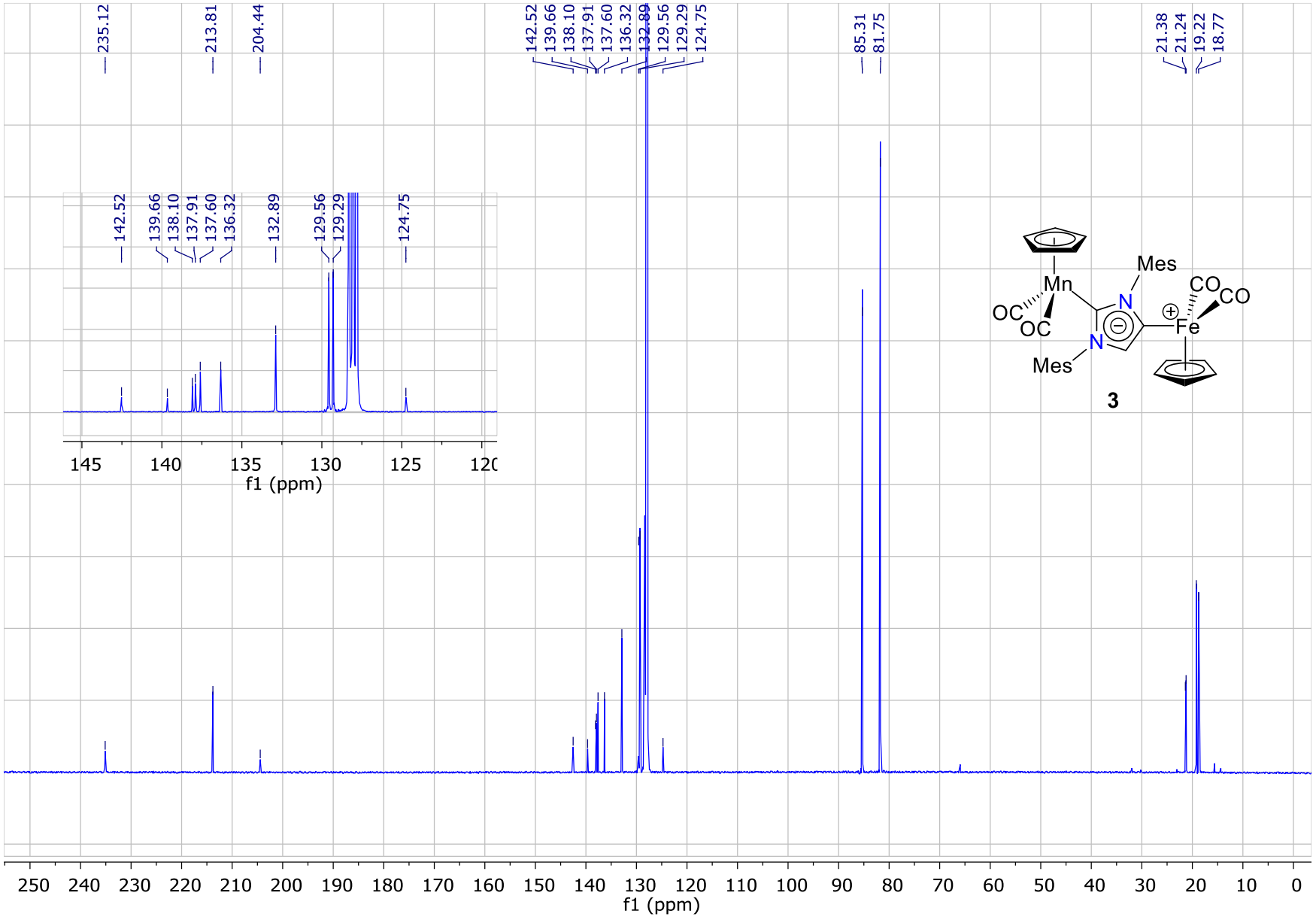


**Figure S2**. $^{13}C\{^{1}H\}$ NMR spectrum of complex **3** (100.6 MHz, $C_6D_6$, 25°C)

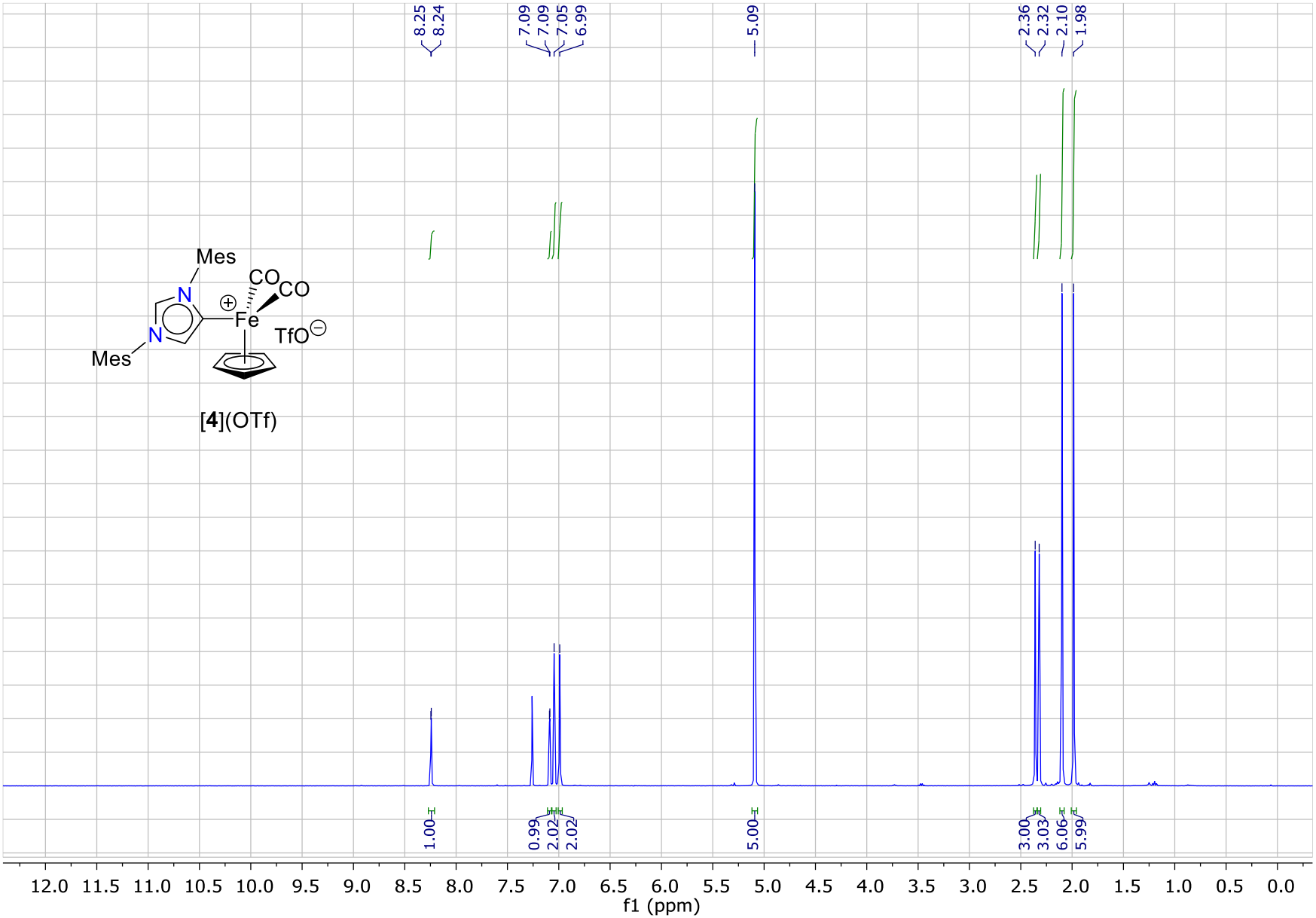


**Figure S3**. $^{1}H$ NMR spectrum of complex [**4**](OTf) (400.1 MHz, $CDCl_3$, 25°C)

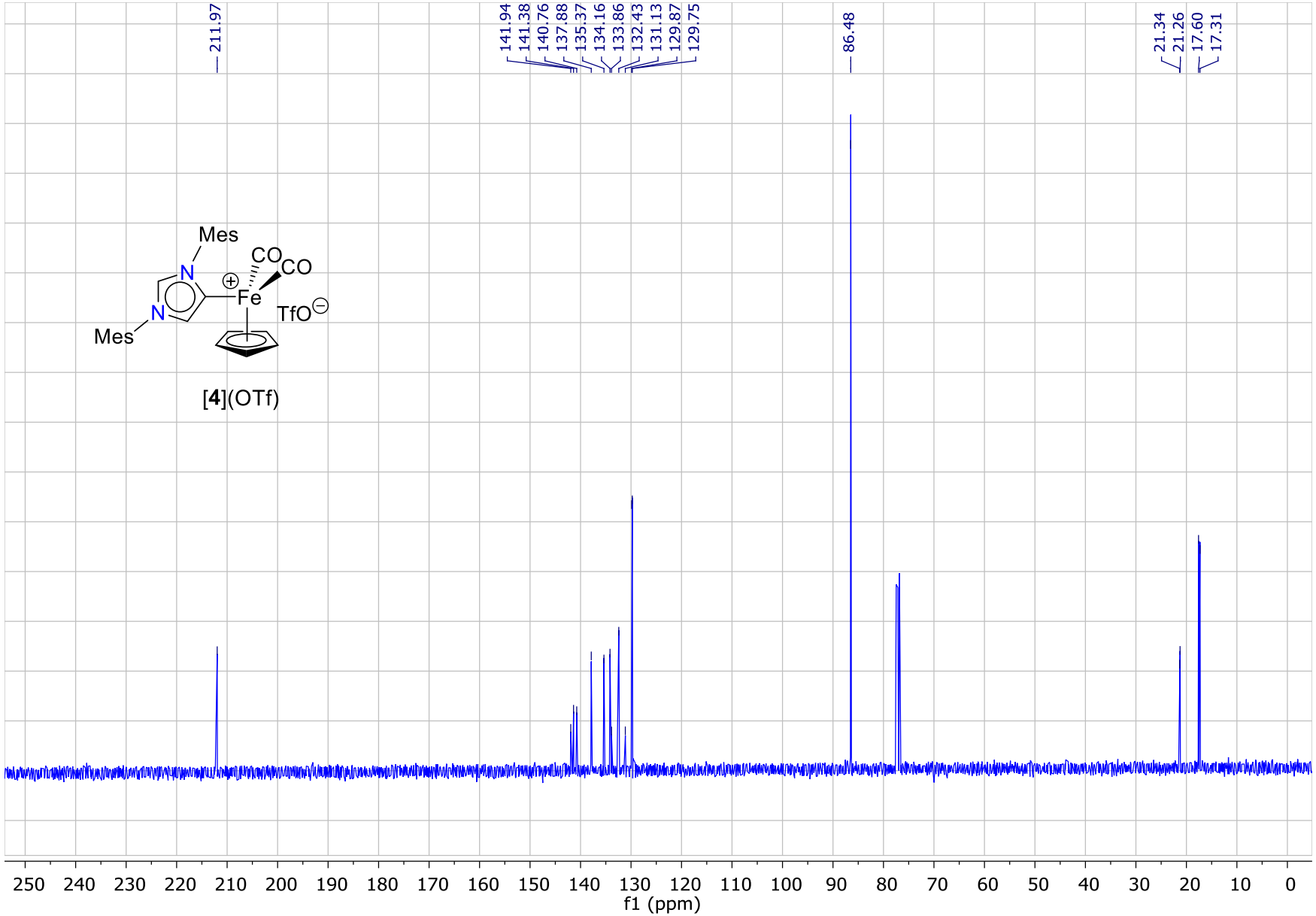


**Figure S4**. $^{13}C\{^{1}H\}$ NMR spectrum of complex [**4**](OTf) (100.6 MHz, $CDCl_3$, 25°C)

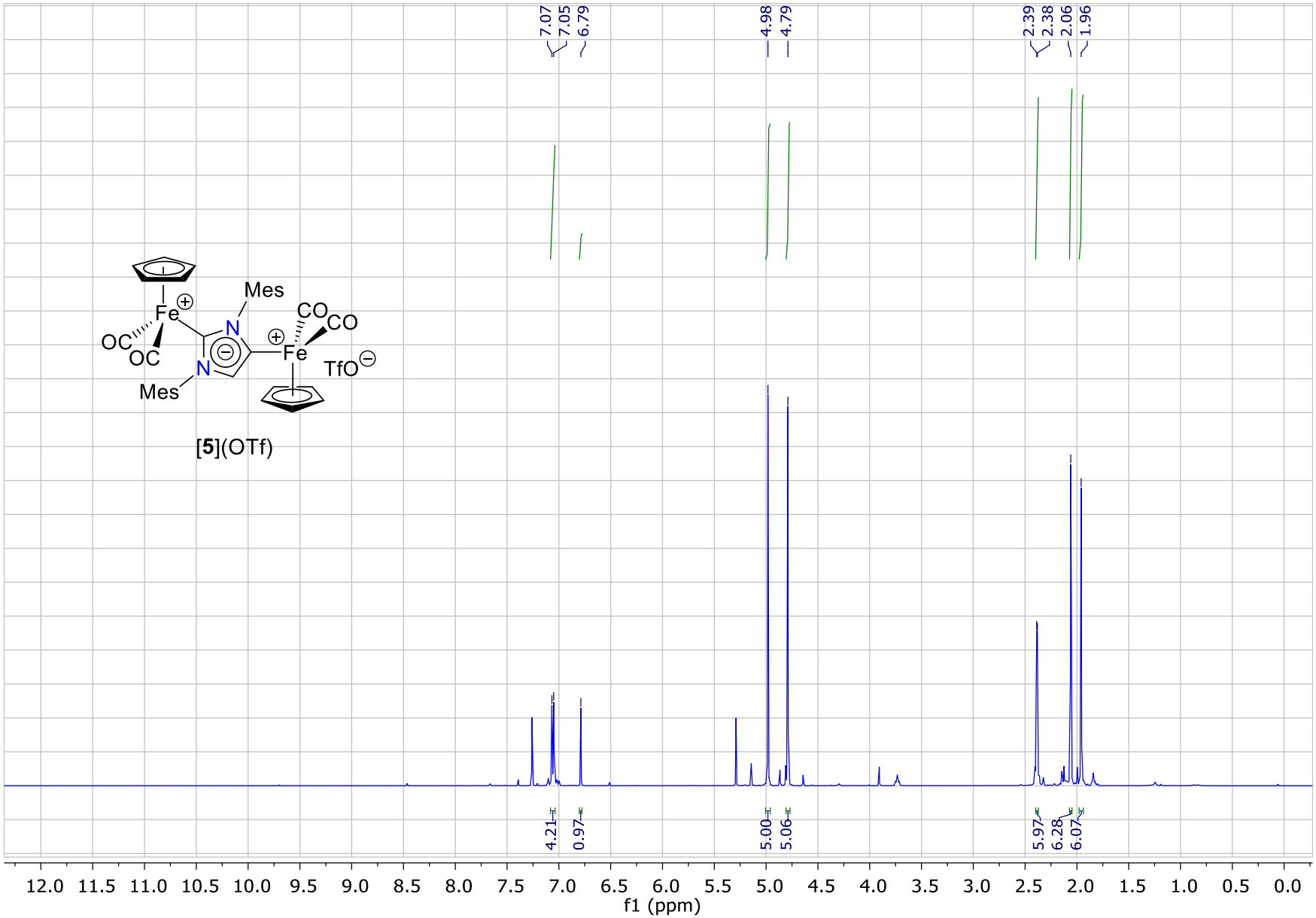


**Figure S5**. $^{1}H$ NMR spectrum of complex [**5**](OTf) (400.1 MHz, $CDCl_3$, 25°C)

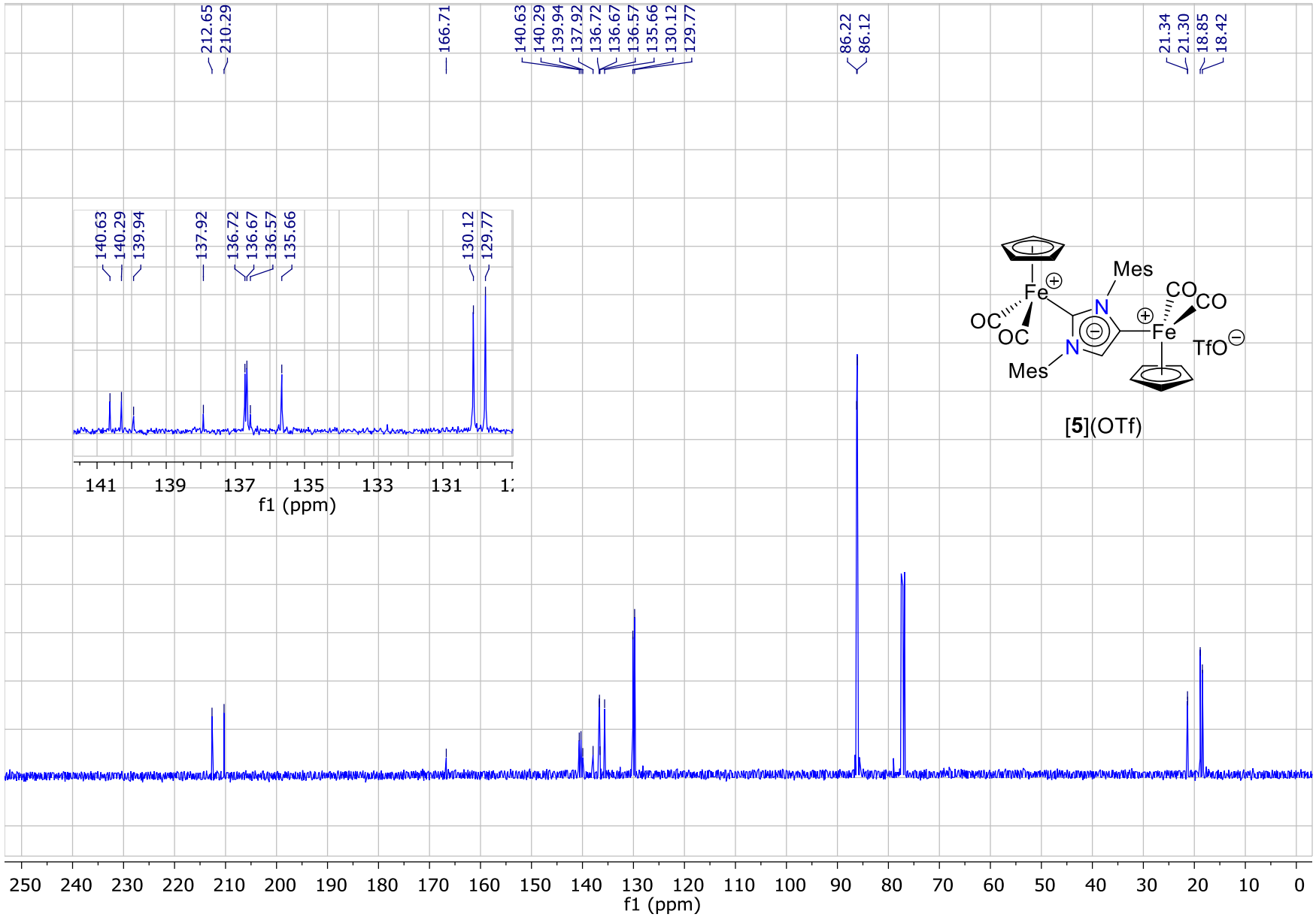


**Figure S6**. $^{13}C\{^{1}H\}$ NMR spectrum of complex [**5**](OTf) (100.6 MHz, $CDCl_3$, 25°C)

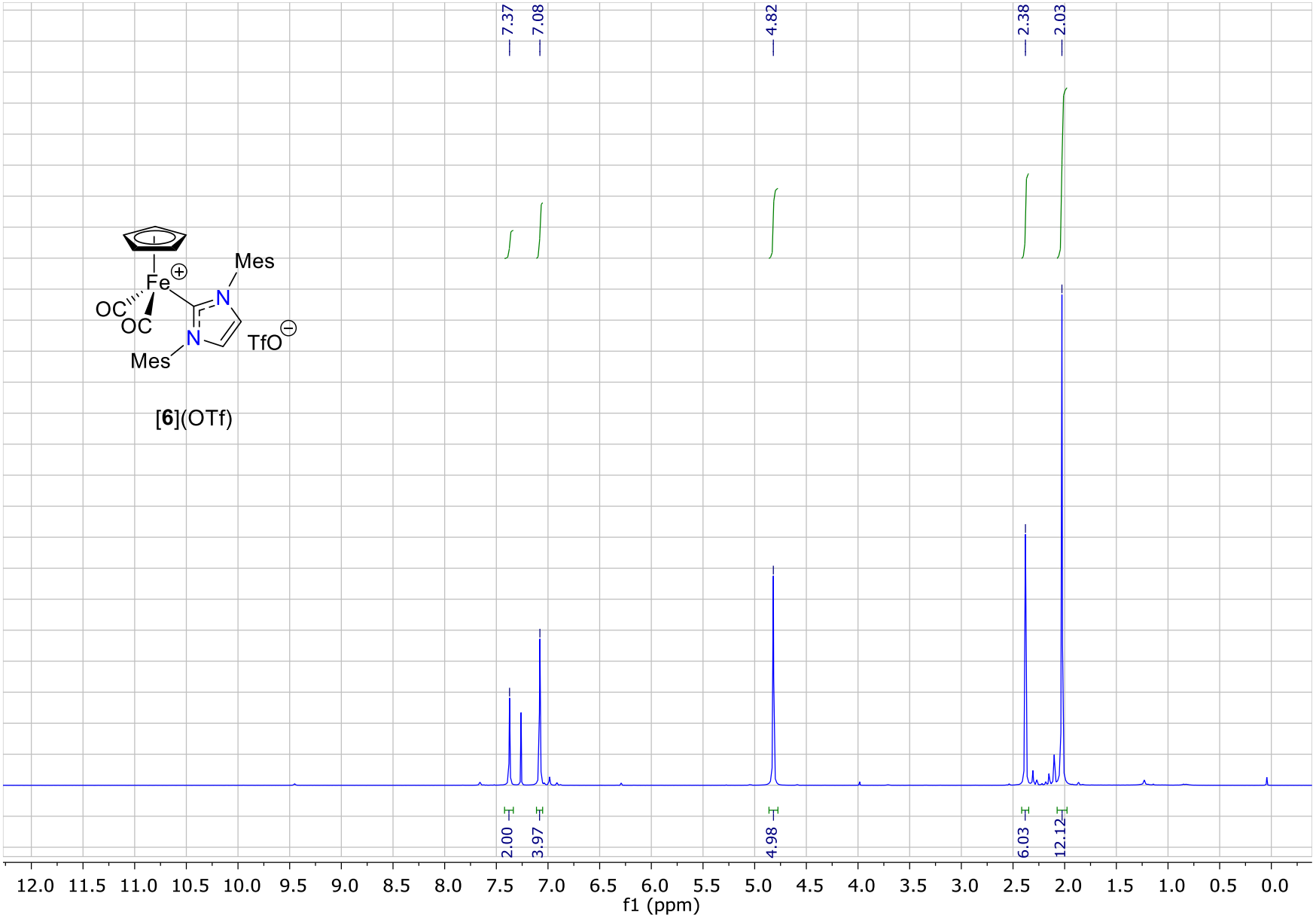


**Figure S7**. $^{1}$H NMR spectrum of complex [**6**](OTf) (400.1 MHz, $CDCl_3$, 25°C)

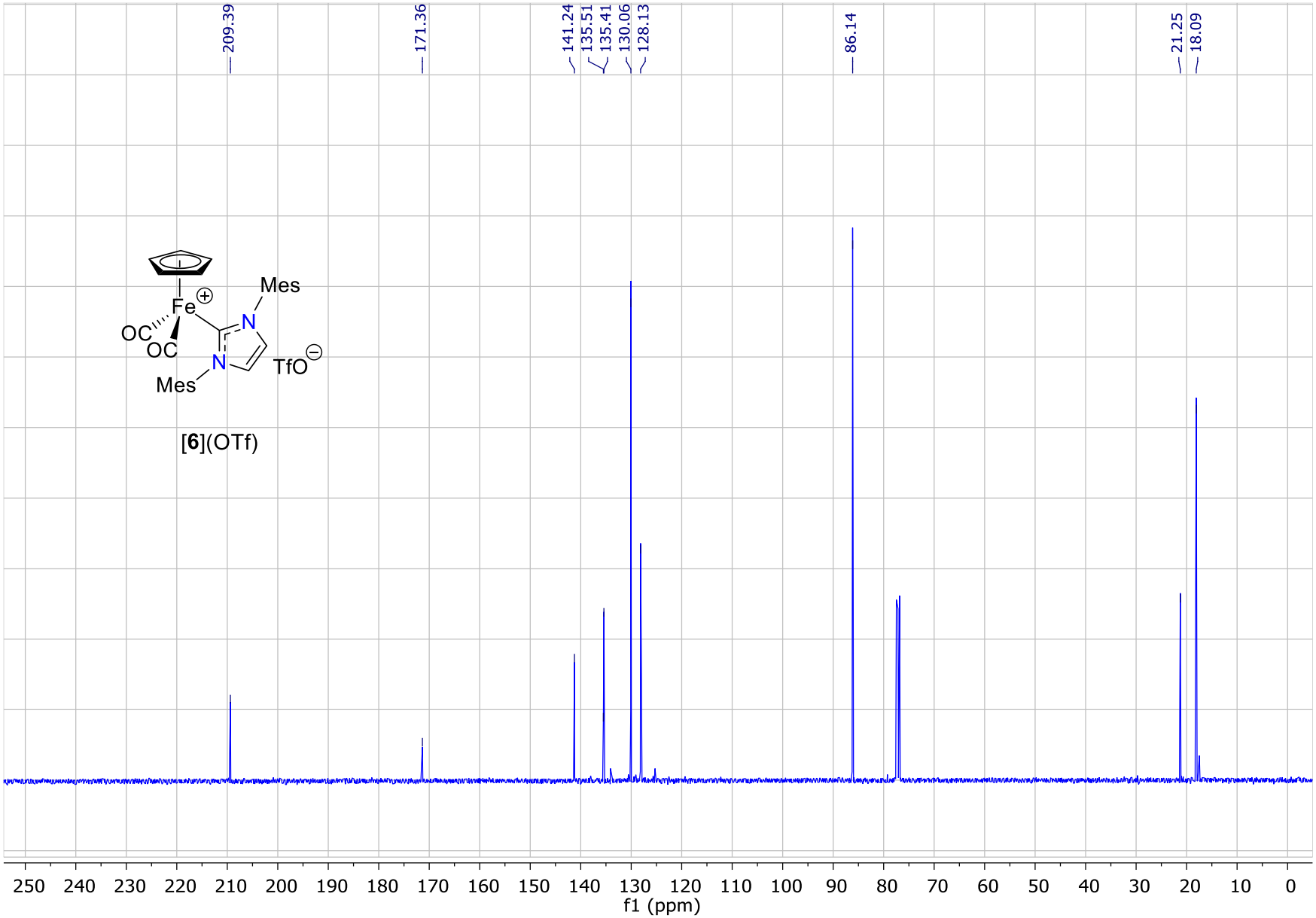


**Figure S8**. $^{13}C\{^{1}H\}$ NMR spectrum of complex [**6**](OTf) (100.6 MHz, $CDCl_3$, 25°C)

## 2. Electrochemical studies of Mn(I) and Fe(II) NHC complexes

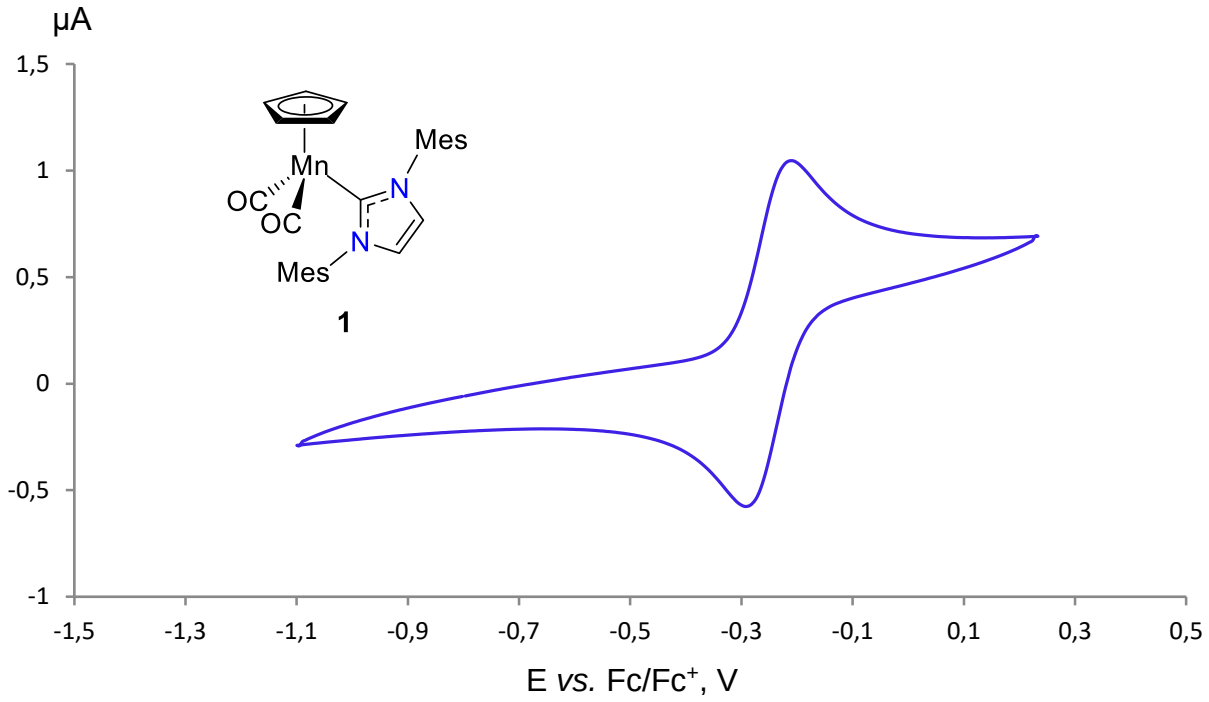


**Figure S9**. Cyclic voltammogram of complex $CpMn(CO)_2(IMes)$ (**1**). Experimental conditions: Pt electrode, MeCN, 1 mM sample concentration, 0.1 M $Bu_4NPF_6$ as supporting electrolyte, 200 mV/s, potentials *vs.* $Fc/Fc^+$ couple.

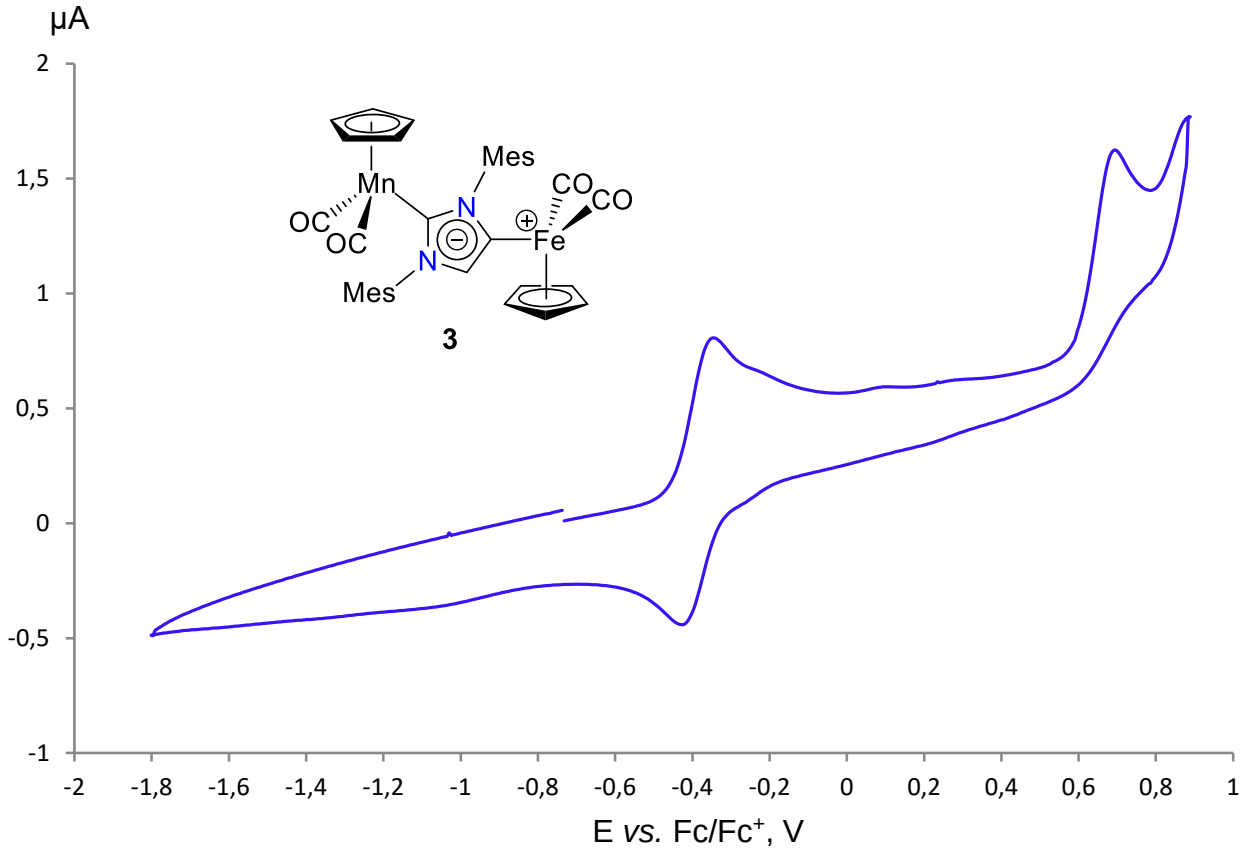


**Figure S10**. Cyclic voltammogram of complex $CpMn(CO)_2(\mu\text{-}d\text{IMes})Fe(CO)_2Cp$ (**3**). Experimental conditions: Pt electrode, MeCN, 1 mM sample concentration, 0.1 M $Bu_4NPF_6$ as supporting electrolyte, 200 mV/s, potentials *vs.* $Fc/Fc^+$ couple.

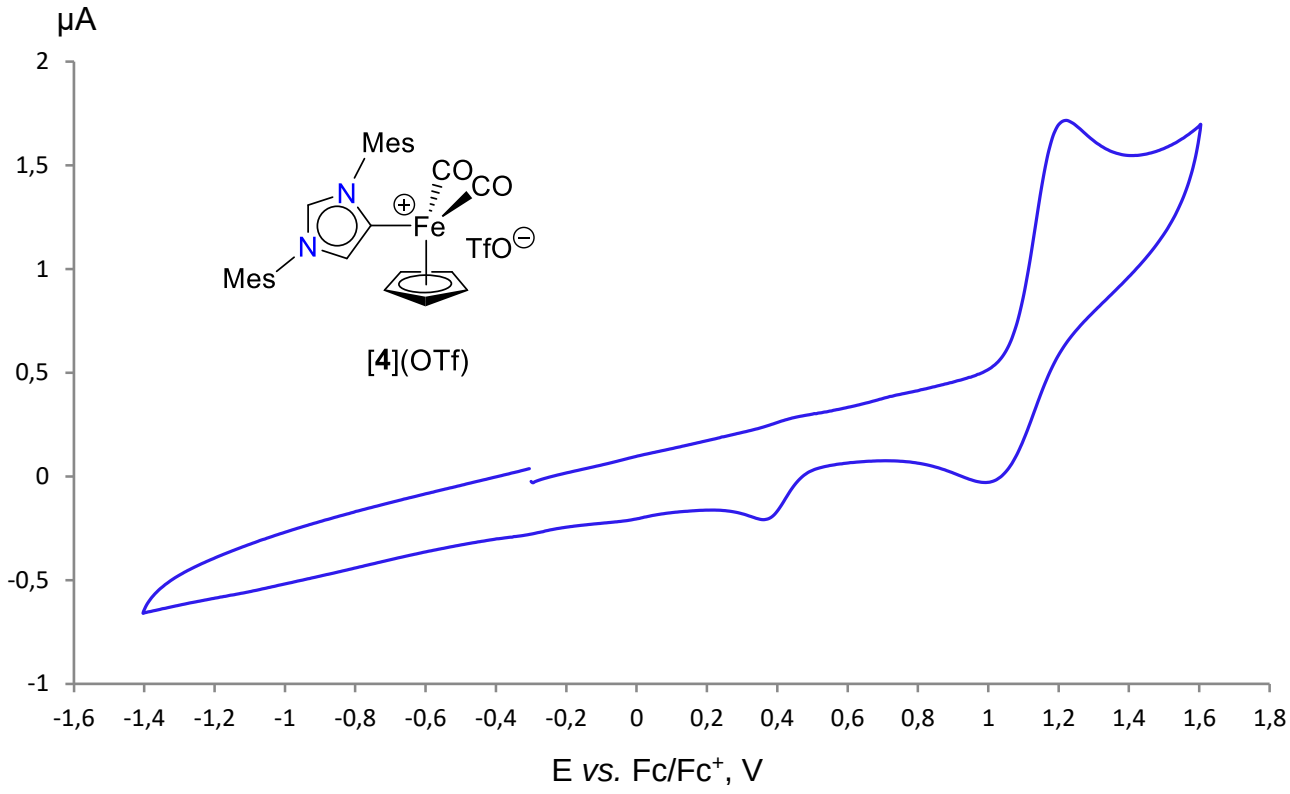


**Figure S11**. Cyclic voltammogram of complex [CpFe(CO)$_2$(*a*IMes)](OTf) ([**4**](OTf)). Experimental conditions: Pt electrode, MeCN, 1 mM sample concentration, 0.1 M $Bu_4NPF_6$ as supporting electrolyte, 200 mV/s, potentials *vs.* Fc/Fc$^+$ couple.

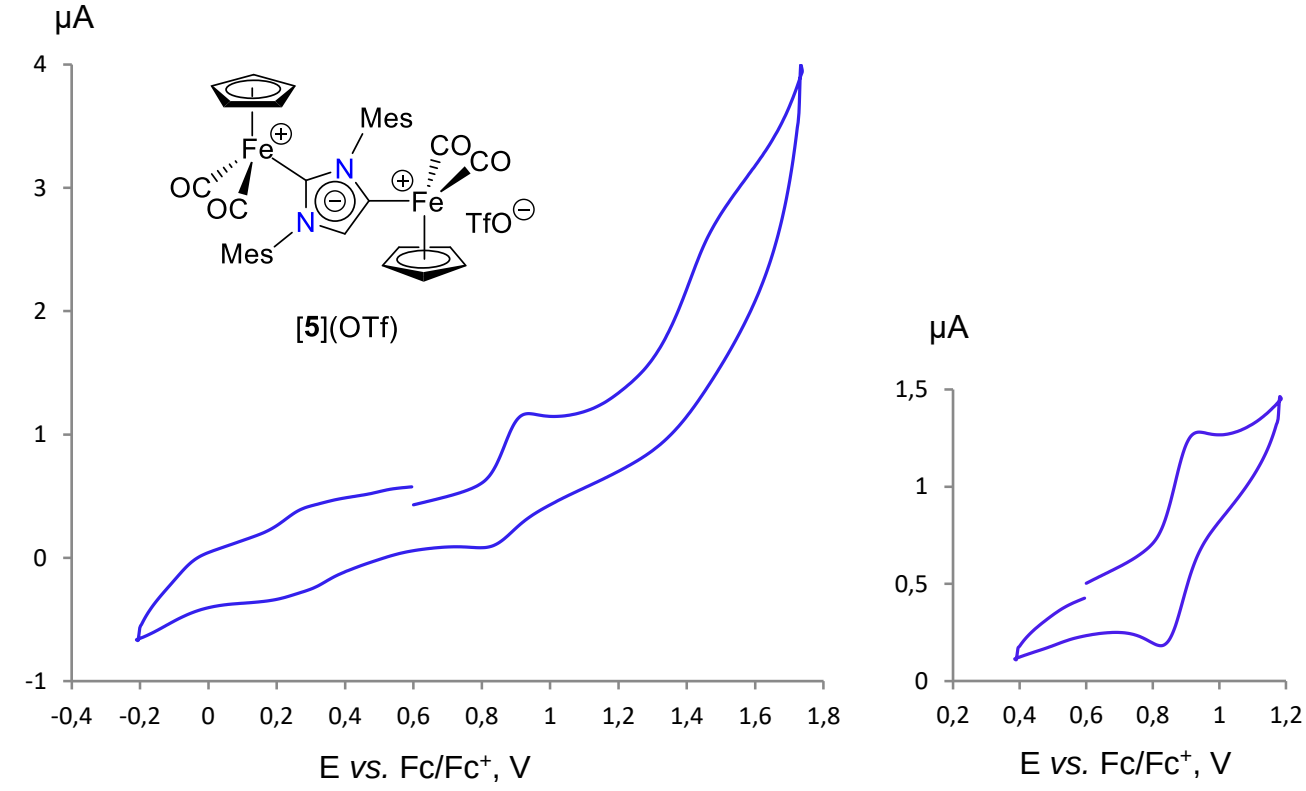


**Figure S12**. Cyclic voltammograms of complex [CpFe(CO)$_2$(*µ-d*IMes)Fe(CO)$_2$Cp](OTf) ([**5**](OTf)). Experimental conditions: Pt electrode, MeCN, 1 mM sample concentration, 0.1 M $Bu_4NPF_6$ as supporting electrolyte, 200 mV/s, potentials *vs.* Fc/Fc$^+$ couple.

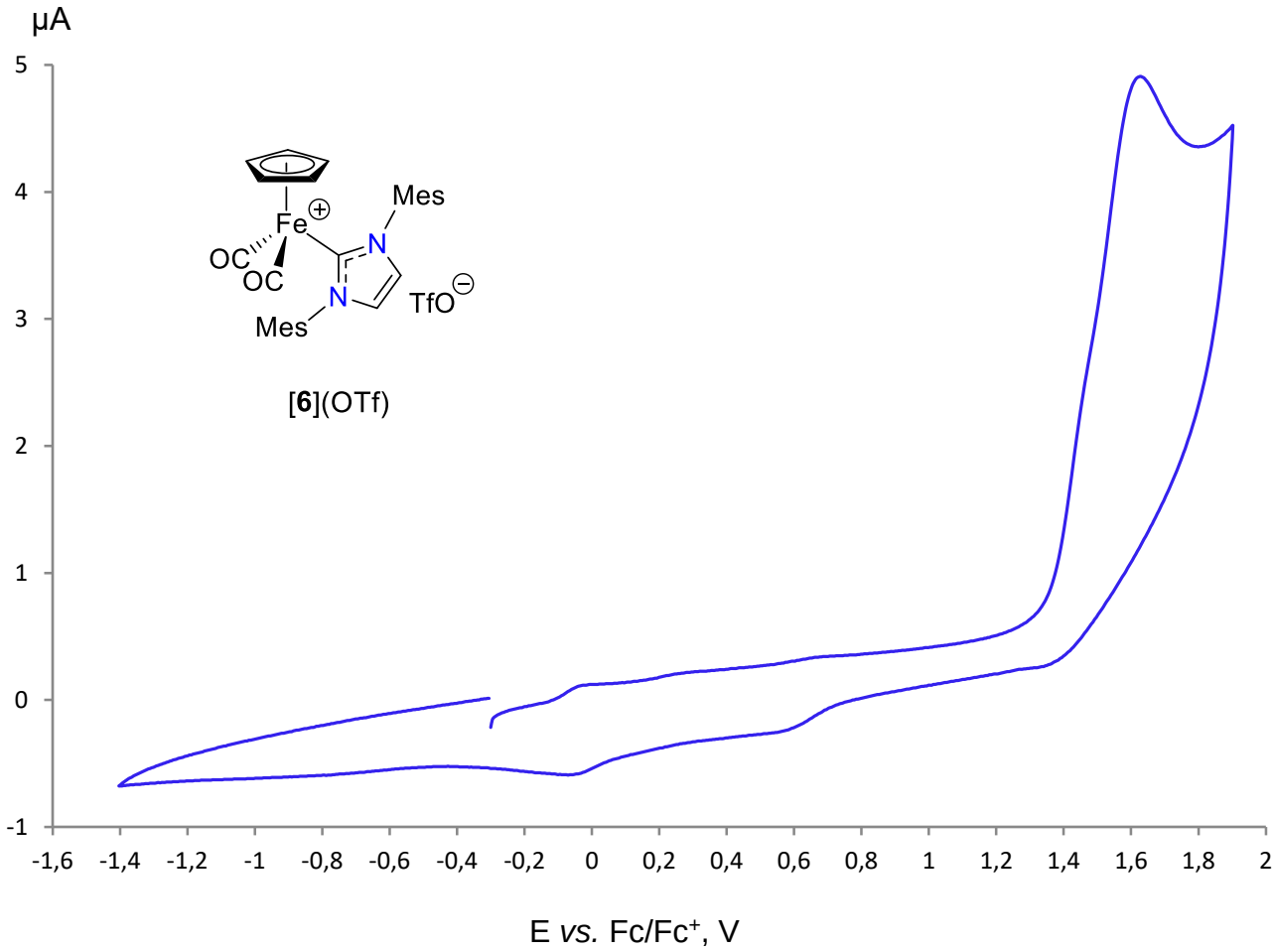


**Figure S13**. Cyclic voltammogram of complex [$CpFe(CO)_2$(IMes)](OTf) ([**6**](OTf)). Experimental conditions: Pt electrode, MeCN, 1 mM sample concentration, 0.1 M $Bu_4NPF_6$ as supporting electrolyte, 200 mV/s, potentials *vs.* $Fc/Fc^+$ couple.2. Electrochemical studies of Mn(I) and Fe(II) NHC complexes

## 3. Computational results

**Table S1.** Key structural data of calculated Mn(I) and Fe(II) NHC complexes (G09/BP86-D3/Def2-TZVP).

| Complex | M1−NHC | $C_{ipso}$...C1−O1 | $C_{ipso}$...C2−O2 | M1−C1−O1 | M1−C2−O2 | M2−*a*NHC | $C_{ipso}$...C3−O3 | M2−C3−O3 | M2−C4−O4 |
|---|---|---|---|---|---|---|---|---|---|
| **1a** | 1.979 Å | 3.288 Å | 3.084 Å | 173.95° | 172.43° | − | − | − | − |
| **1b** | 1.980 Å | 3.938 Å | 2.850 Å | 177.28° | 169.34° | − | − | − | − |
| **6a**$^+$ | 1.976 Å | 3.305 Å | 2.965 Å | 174.32° | 171.00° | − | − | − | − |
| **6b**$^+$ | 1.984 Å | 3.820 Å | 2.788 Å | 176.60° | 167.16° | − | − | − | − |
| **4**$^+$ | − | − | − | − | − | 1.967 Å | 2.915 Å | 170.84° | 179.04° |
| **3a** | 1.988 Å | 3.299 Å | 3.046 Å | 174.09 Å | 172.07 Å | 1.982 Å | 2.932 Å | 170.51° | 179.67° |
| **3b** | 1.992 Å | 3.840 Å | 2.840 Å | 176.79° | 169.14° | 1.987 Å | 2.894 Å | 169.34° | 179.39° |
| **5a**$^+$ | 1.985 Å | 3.308 Å | 2.934 Å | 174.08° | 170.55° | 1.977 Å | 2.920 Å | 171.29° | 178.99° |
| **5b**$^+$ | 1.995 Å | 3.749 Å | 2.779 Å | 176.53° | 166.96° | 1.981 Å | 2.891 Å | 170.52° | 178.95° |

**Table S2.** Energy difference between the conformers Mn(I) and Fe(II) NHC complexes (G09/BP86-D3/Def2-TZVP, horizontal isomers are taken as zero).

| Complex | **1a/1b** | **6a**$^+$**/6b**$^+$ | **3a/3b** | **5a**$^+$**/5b**$^+$ |
|---|---|---|---|---|
| ΔE, kcal mol$^{-1}$ | −0.70 | −0.29 | 0.06 | −0.07 |
| $\Delta E_{ZPE}$, kcal mol$^{-1}$ | −0.67 | −0.24 | 0.05 | −0.10 |
| $\Delta E_{thermal}$, kcal mol$^{-1}$ | −0.70 | −0.30 | −0.53 | −0.09 |
| $\Delta H^{298}$, kcal mol$^{-1}$ | −0.70 | −0.30 | −0.53 | −0.09 |
| $\Delta G^{298}$, kcal mol$^{-1}$ | −0.46 | 0.93 | 1.63 | 0.35 |
| $\Delta S^{298}$, cal·mol$^{-1}$·K$^{-1}$ | −0.83 | −4.10 | −7.24 | −1.48 |

**Table S3.** Characteristics of BCPs for π(C=C)...π*(C≡O) interligand interactions in optimized Mn(I) and Fe(II) NHC complexes (G09/BP86-D3/Def2-TZVP).[a]

| Complex | **1a** | **1b** | **6a**$^+$ | **6b**$^+$ | **4**$^+$ | **3a** NHC | **3a** *a*NHC | **3b** NHC | **3b** *a*NHC | **5a**$^+$ NHC | **5a**$^+$ *a*NHC | **5b**$^+$ NHC | **5b**$^+$ *a*NHC |
|---|---|---|---|---|---|---|---|---|---|---|---|---|---|
| $\rho_c$ | − | 0.014 | 0.012 | 0.016 | 0.013 | − | 0.012 | 0.014 | 0.013 | 0.012 | 0.013 | 0.016 | 0.013 |
| $\nabla^2(\rho_c)$ | − | 0.038 | 0.032 | 0.041 | 0.034 | − | 0.033 | 0.039 | 0.035 | 0.034 | 0.034 | 0.042 | 0.036 |
| $\varepsilon_c$ | − | 0.200 | 1.303 | 0.088 | 0.287 | − | 0.266 | 0.240 | 0.155 | 1.074 | 0.258 | 0.122 | 0.179 |
| $V_c$ | − | −0.008 | −0.006 | −0.008 | −0.006 | − | −0.006 | −0.008 | −0.007 | −0.006 | −0.007 | −0.008 | −0.007 |
| $G_c$ | − | 0.009 | 0.007 | 0.009 | 0.007 | − | 0.007 | 0.009 | 0.008 | 0.007 | 0.008 | 0.009 | 0.008 |
| $K_c$ | − | −0.001 | −0.001 | −0.001 | −0.001 | − | −0.001 | −0.001 | −0.001 | −0.001 | −0.001 | −0.001 | −0.001 |
| $L_c$ | − | −0.010 | −0.008 | −0.010 | −0.008 | − | −0.008 | −0.010 | −0.009 | −0.008 | −0.009 | −0.010 | −0.009 |
| DI | − | 0.043 | 0.035 | 0.054 | 0.038 | − | 0.037 | 0.043 | 0.041 | 0.037 | 0.036 | 0.053 | 0.039 |
| $E_{BCP}$ | − | −2.4 | −1.9 | −2.6 | −2.0 | − | −2.0 | −2.4 | −2.1 | −2.0 | −2.1 | −2.6 | −2.2 |

[a] $\rho_c$ – electron density at BCP, a.u.; ε – bond ellipticity; $\nabla^2(\rho_c)$ - Laplacian of Rho = trace of hessian of Rho; V = virial field = potential energy density = trace of stress tensor; G = Lagrangian form of kinetic energy density; K = Hamiltonian form of kinetic energy density = L = K − G = Lagrangian density = (−1/4) $\nabla^2(\rho_c)$; DI = delocalization index = bond order; $E_{BCP}$ – energy of interaction, kcal mol$^{-1}$.

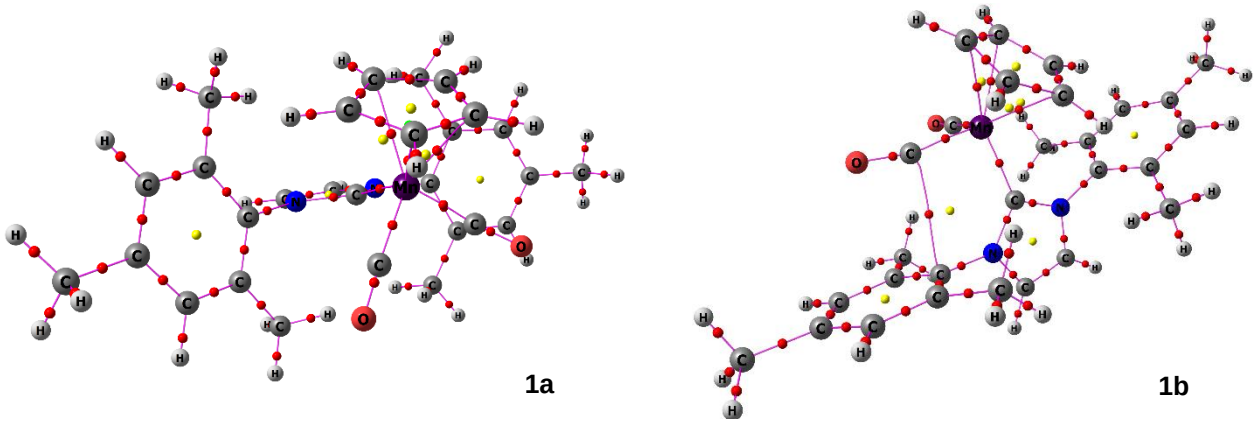


**Figure S14.** Molecular graphs for Mn(I) IMes complexes **1a** (left) and **1b** (right). Weak C−H···H−C and C−H···C≡O interactions with the energies below 1.5 kcal mol$^{-1}$ are not shown for clarity. Pink – bond paths', red balls – bond (3,−1) critical points, yellow balls − ring (3,+1) critical points, green balls – cage (3,+3) critical points.

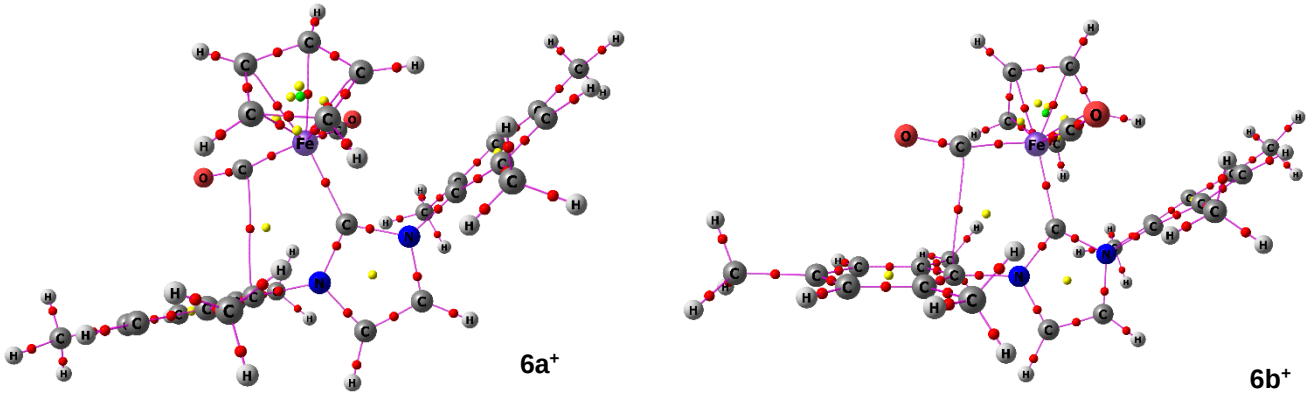


**Figure S15.** Molecular graphs for Fe(II) IMes complexes **6a**$^+$ (left) and **6a**$^+$ (right). Weak C−H···H−C and C−H···C≡O interactions with the energies below 1.5 kcal mol$^{-1}$ are not shown for clarity. Pink – bond paths', red balls – bond (3,−1) critical points, yellow balls − ring (3,+1) critical points, green balls – cage (3,+3) critical points.

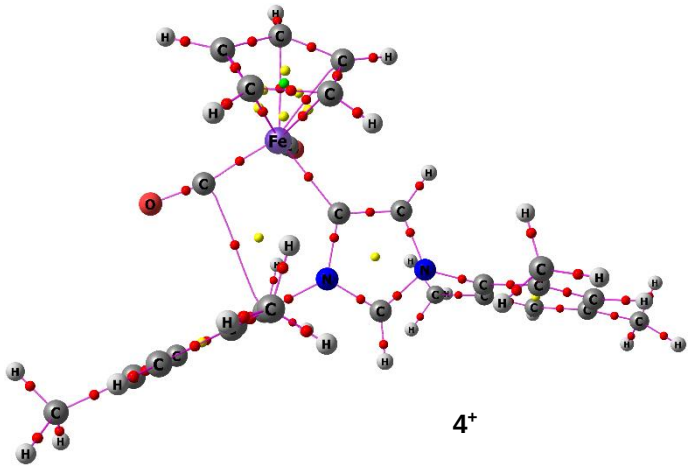


**Figure S16.** Molecular graphs for Fe(II) *a*IMes complex **4**$^+$. Weak C−H···H−C and C−H···C≡O interactions with the energies below 1.5 kcal mol$^{-1}$ are not shown for clarity. Pink – bond paths', red balls – bond (3,−1) critical points, yellow balls − ring (3,+1) critical points, green balls – cage (3,+3) critical points.

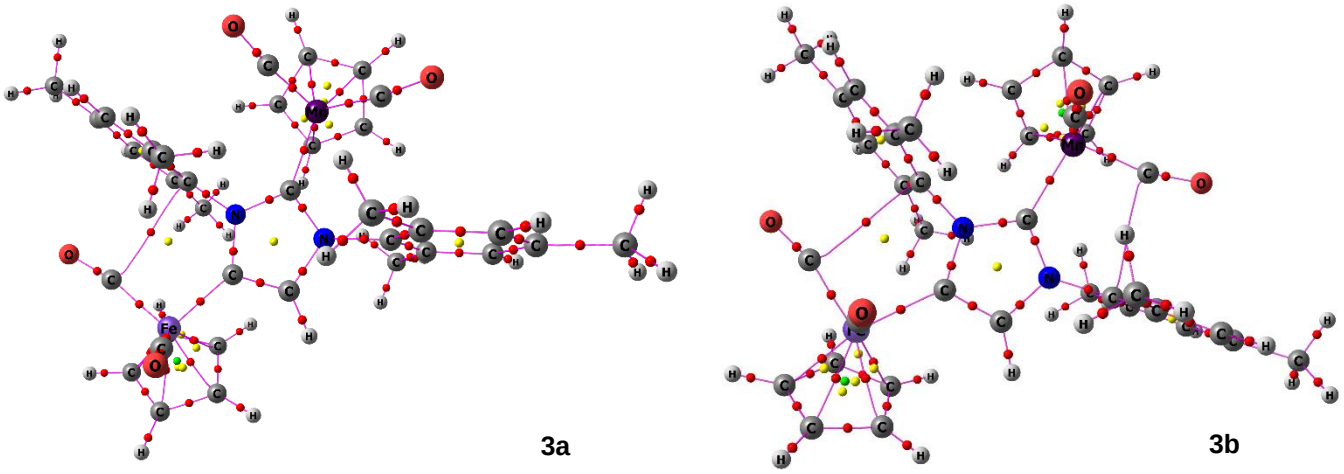


**Figure S17.** Molecular graphs for Mn(I)/Fe(II) *d*IMes complexes **3a** (left) and **3b** (right). Weak C−H···H−C and C−H···C≡O interactions with the energies below 1.5 kcal mol$^{-1}$ are not shown for clarity. Pink – bond paths', red balls – bond (3,−1) critical points, yellow balls − ring (3,+1) critical points, green balls – cage (3,+3) critical points.

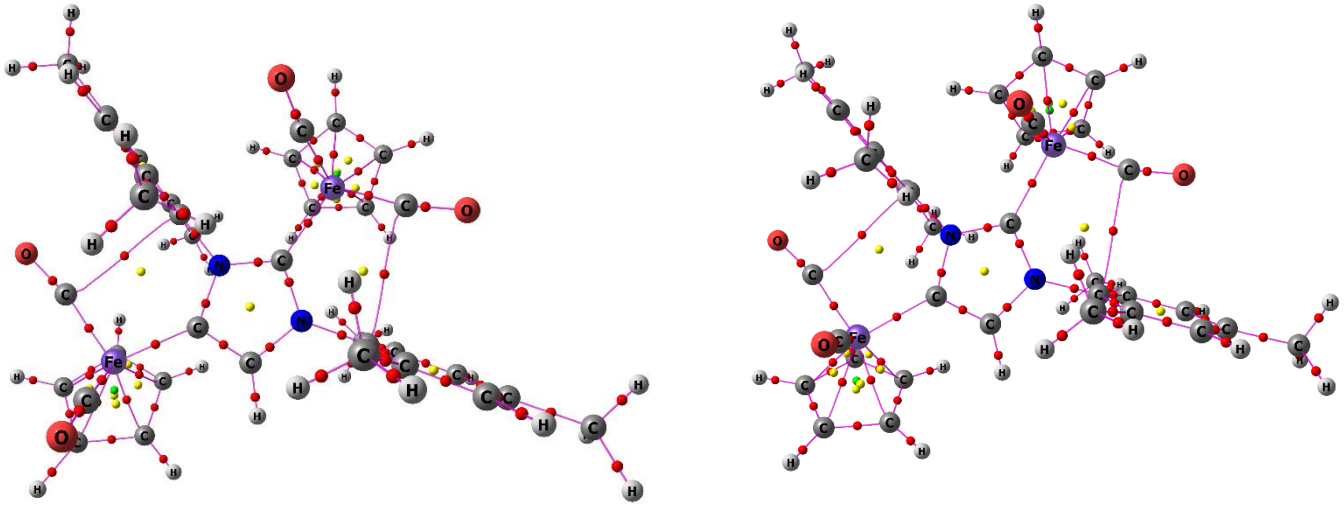

**Figure S18.** Molecular graphs for Fe(II) *d*IMes complexes **5a**$^{+}$ (left) and **5b**$^{+}$ (right). Weak C−H···H−C and C−H···C≡O interactions with the energies below 1.5 kcal mol$^{-1}$ are not shown for clarity. Pink – bond paths', red balls – bond (3,−1) critical points, yellow balls − ring (3,+1) critical points, green balls – cage (3,+3) critical points.

**Table S4.** Characteristics of BCPs for metal-carbene bonds in optimized Mn(I) and Fe(II) NHC complexes (G09/BP86-D3/Def2-TZVP).[a]

| Complex | **1a** NHC | **1b** NHC | **6a**$^+$ NHC | **6b**$^+$ NHC | **4**$^+$ *a*NHC | **3a** NHC | **3a** *a*NHC | **3b** NHC | **3b** *a*NHC | **5a**$^+$ NHC | **5a**$^+$ *a*NHC | **5b**$^+$ NHC | **5b**$^+$ *a*NHC |
|---|---|---|---|---|---|---|---|---|---|---|---|---|---|
| $\rho_c$ | 0.108 | 0.107 | 0.111 | 0.109 | 0.114 | 0.107 | 0.112 | 0.104 | 0.111 | 0.110 | 0.112 | 0.106 | 0.111 |
| $\nabla^2(\rho_c)$ | 0.301 | 0.314 | 0.238 | 0.243 | 0.215 | 0.289 | 0.168 | 0.303 | 0.168 | 0.222 | 0.196 | 0.227 | 0.195 |
| $\varepsilon_c$ | 0.036 | 0.086 | 0.022 | 0.056 | 0.065 | 0.037 | 0.057 | 0.081 | 0.081 | 0.024 | 0.066 | 0.056 | 0.082 |
| $V_c$ | −0.146 | −0.147 | −0.144 | −0.141 | −0.145 | −0.142 | −0.133 | −0.141 | −0.131 | −0.139 | −0.138 | −0.135 | −0.137 |
| $G_c$ | 0.111 | 0.113 | 0.102 | 0.101 | 0.099 | 0.107 | 0.088 | 0.108 | 0.087 | 0.097 | 0.094 | 0.096 | 0.093 |
| $K_c$ | 0.036 | 0.034 | 0.042 | 0.040 | 0.045 | 0.035 | 0.046 | 0.033 | 0.045 | 0.042 | 0.045 | 0.039 | 0.044 |
| $L_c$ | −0.075 | −0.079 | −0.060 | −0.061 | −0.054 | −0.072 | −0.042 | −0.076 | −0.042 | −0.055 | −0.049 | −0.057 | −0.049 |
| DI | 0.800 | 0.813 | 0.782 | 0.779 | 0.799 | 0.787 | 0.791 | 0.795 | 0.787 | 0.776 | 0.792 | 0.769 | 0.789 |

[a] $\rho_c$ – electron density at BCP, a.u.; ε – bond ellipticity; $\nabla^2(\rho_c)$ - Laplacian of Rho = trace of hessian of Rho; V = virial field = potential energy density = trace of stress tensor; G = Lagrangian form of kinetic energy density; K = Hamiltonian form of kinetic energy density = L = K − G = Lagrangian density = (−1/4) $\nabla^2(\rho_c)$; DI = delocalization index = bond order.

**Table S5.** Selected AIM charges for optimized Mn(I) and Fe(II) NHC complexes.

| Complex | **1a** | **1b** | **6a**$^+$ | **6b**$^+$ | **4**$^+$ | **3a** | **3b** | **5a**$^+$ | **5b**$^+$ |
|---|---|---|---|---|---|---|---|---|---|
| M−NHC | +0.948 | +0.946 | +0.845 | +0.843 | − | +0.951 | +0.947 | +0.845 | +0.844 |
| M−*a*NHC | − | − | − | − | +0.840 | +0.838 | +0.840 | +0.840 | +0.841 |
| $CpM(CO)_2$−NHC[a] | −0.142 | −0.134 | +0.561 | +0.550 | − | −0.157 | −0.151 | +0.523 | +0.514 |
| $CpM(CO)_2$−*a*NHC[a] | − | − | − | − | +0.502 | +0.345 | +0.344 | +0.456 | +0.457 |
| NHC[b] | −0.799 | −0.806 | −0.647 | −0.649 | −0.616 | −1.115 | −1.123 | −1.027 | −1.031 |
| C2 | +0.601 | +0.590 | +0.660 | +0.653 | +0.872 | +0.596 | +0.587 | +0.649 | +0.642 |
| C4 | +0.286[c] | +0.286[c] | +0.308[c] | +0.309[c] | +0.178 | +0.142 | +0.141 | +0.154 | +0.156 |

[a] total AIM charge of the $Cp(CO)_2M$ moiety
[b] total AIM charge of the heterocyclic moiety without aryl groups ($C_3N_2H_2$ and $C_3N_2H_1$ for mono- and ditopic carbenes, respectively)
[c] for normal carbene complexes average charge of C4 and C5 is provided due to slight asymmetry

**Table S6.** Selected NBO6 charges for optimized Mn(I) and Fe(II) NHC complexes (G09/BP86-D3/Def2-TZVP).

| Complex | **1a** | **1b** | **6a**$^+$ | **6b**$^+$ | **4**$^+$ | **3a** | **3b** | **5a**$^+$ | **5b**$^+$ |
|---|---|---|---|---|---|---|---|---|---|
| M−NHC | −0.576 | −0.565 | −0.241 | −0.230 | − | −0.570 | −0.557 | −0.238 | −0.226 |
| M−*a*NHC | − | − | − | − | −0.240 | −0.239 | −0.235 | −0.239 | −0.236 |
| $CpM(CO)_2$−NHC[a] | −0.386 | −0.373 | +0.441 | +0.446 | − | −0.392 | −0.380 | +0.416 | +0.412 |
| $CpM(CO)_2$−*a*NHC[a] | − | − | − | − | +0.394 | +0.271 | +0.272 | +0.362 | +0.364 |
| NHC[b] | −0.099 | −0.111 | −0.007 | −0.015 | 0.019 | −0.358 | −0.375 | −0.322 | −0.334 |
| C2 | +0.407 | +0.393 | +0.377 | +0.365 | +0.191 | +0.394 | +0.381 | +0.361 | +0.346 |
| C4 | −0.101[c] | −0.100[c] | −0.079[c] | −0.077[c] | +0.097 | +0.079 | +0.075 | +0.081 | +0.082 |

[a] total NBO charge of the $Cp(CO)_2M$ moiety
[b] total NBO charge of the heterocyclic moiety without aryl groups ($C_3N_2H_2$ and $C_3N_2H_1$ for mono- and ditopic carbenes, respectively)
[c] for normal carbene complexes average charge of C4 and C5 is provided due to slight asymmetry

**Table S7**. Calculated $\nu_{CO}$ bands for optimized Mn(I) and Fe(II) NHC complexes.

| Complex | **1a** | **1b** | **6a**$^+$ | **6b**$^+$ | **4**$^+$ | **3a** M−NHC | **3a** M−*a*NHC | **3b** M−NHC | **3b** M−*a*NHC | **5a**$^+$ M−NHC | **5a**$^+$ M−*a*NHC | **5b**$^+$ M−NHC | **5b**$^+$ M−*a*NHC |
|---|---|---|---|---|---|---|---|---|---|---|---|---|---|
| G09[a] | | | | | | | | | | | | | |
| $\nu_1$, cm$^{-1}$ | 1875 | 1872 | 1999 | 1993 | 1993 | 1873 | 1975 | 1869 | 1974 | 1994 | 1986 | 1987 | 1984 |
| $A_1$, km mol$^{-1}$ | 831 | 669 | 564 | 476 | 524 | 740 | 523 | 615 | 504 | 639 | 364 | 408 | 482 |
| $\nu_2$, cm$^{-1}$ | 1923 | 1922 | 2038 | 2031 | 2033 | 1919 | 2017 | 1918 | 2016 | 2034 | 2026 | 2029 | 2023 |
| $A_2$, km mol$^{-1}$ | 558 | 627 | 390 | 407 | 438 | 621 | 492 | 652 | 449 | 618 | 243 | 609 | 265 |
| ΔG09,[b] cm$^{-1}$ | | | | | | | | | | | | | |
| $\nu_1$ | −39 | −36 | 7 | 14 | 3 | −46 | 5 | −42 | 6 | 4 | 5 | 11 | 7 |
| $\nu_2$ | −15 | −14 | 13 | 19 | 11 | −19 | 13 | −17 | 14 | 10 | 12 | 15 | 14 |
| ADF[c] | | | | | | | | | | | | | |
| $\nu_1$, cm$^{-1}$ | 1854 | 1851 | 1979 | 1972 | 1973 | 1850 | 1954 | 1848 | 1953 | 1973 | 1964 | 1963 | 1966 |
| $A_1$, km mol$^{-1}$ | 860 | 698 | 582 | 493 | 556 | 773 | 564 | 641 | 528 | 658 | 396 | 516 | 388 |
| $\nu_2$, cm$^{-1}$ | 1903 | 1903 | 2018 | 2011 | 2013 | 1898 | 1996 | 1898 | 1996 | 2015 | 2005 | 2002 | 2009 |
| $A_2$, km mol$^{-1}$ | 591 | 646 | 417 | 422 | 457 | 659 | 515 | 673 | 472 | 649 | 264 | 315 | 599 |
| ΔADF,[b] cm$^{-1}$ | | | | | | | | | | | | | |
| $\nu_1$ | −18 | −15 | 28 | 34 | 23 | −23 | 26 | −21 | 27 | 25 | 27 | 35 | 25 |
| $\nu_2$ | 6 | 6 | 32 | 39 | 31 | 2 | 34 | 3 | 34 | 29 | 33 | 42 | 29 |

[a] G09/BP86-D3/Def2-TZVP level.

[b] $\Delta = \nu_{CO}^{exp} - \nu_{CO}^{calc}$

[c] ADF/BP86-D3/TZP level.

**Table S8**. ETS-NOCV analysis data for metal-carbene bonding in optimized Mn(I) and Fe(II) NHC complexes bearing IMes, *a*IMes and *d*IMes ligands (ADF/BP86-D3/TZP, energies are given in kcal mol$^{-1}$).

| Complex | **1a** | **1b** | **6a**$^+$ | **6b**$^+$ | **4**$^+$ | **3a** M−NHC | **3a** M−*a*NHC | **3b** M−NHC | **3b** M−*a*NHC | **5a**$^+$ M−NHC | **5a**$^+$ M−*a*NHC | **5b**$^+$ M−NHC | **5b**$^+$ M−*a*NHC |
|---|---|---|---|---|---|---|---|---|---|---|---|---|---|
| $E_{Pauli}$ | 141.5 | 146.2 | 144.1 | 145.1 | 155.3 | 139.1 | 172.7 | 144.7 | 173.0 | 141.7 | 150.5 | 145.5 | 149.9 |
| $E_{elst}$ | −126.4 | −129.5 | −145.3 | −144.9 | −160.9 | −123.5 | −229.3 | −127.5 | −228.7 | −145.6 | −154.8 | −146.5 | −153.2 |
| $E_{disp}$ | −22.9 | −23.6 | −23.8 | −24.1 | −16.0 | −23.7 | −17.4 | −24.3 | −17.4 | −24.7 | −17.2 | −24.9 | −17.4 |
| $E_{int}$ | −73.6 | −75.3 | −112.7 | −113.1 | −117.5 | −73.8 | −188.9 | −75.6 | −188.6 | −120.1 | −125.2 | −120.3 | −124.6 |
| $E_{orb}$ | −65.8 | −68.5 | −87.8 | −89.2 | −95.9 | −65.8 | −114.9 | −68.5 | −115.4 | −91.6 | −103.6 | −94.4 | −103.8 |
| $E_{steric} = E_{Pauli} + E_{elst}$ | 15.1 | 16.7 | −1.2 | 0.2 | −5.6 | 15.6 | −56.6 | 17.2 | −55.7 | −3.9 | −4.3 | −1.0 | −3.3 |
| $E_{orb}/E_{int}$ | 0.89 | 0.91 | 0.78 | 0.79 | 0.82 | 0.89 | 0.61 | 0.91 | 0.61 | 0.76 | 0.83 | 0.78 | 0.83 |
| $E_{elstat}/E_{int}$ | 1.72 | 1.72 | 1.29 | 1.28 | 1.37 | 1.67 | 1.21 | 1.69 | 1.21 | 1.21 | 1.24 | 1.22 | 1.23 |
| $E_{\sigma}$ (C:→M) | −38.0 | −38.8 | −54.3 | −53.9 | −64.8 | −38.6 | −78.2 | −39.4 | −77.9 | −57.3 | −71.5 | −57.5 | −71.3 |
| $E_{\sigma}$ (C:→M)/$E_{orb}$ | 0.58 | 0.57 | 0.62 | 0.60 | 0.68 | 0.59 | 0.68 | 0.58 | 0.68 | 0.63 | 0.69 | 0.61 | 0.69 |
| $E_{\pi\perp}$ (M→C:) | −12.5 | −13.9 | −9.6 | −9.8 | −9.1 | −11.2 | −8.7 | −12.9 | −8.9 | −9.2 | −8.7 | −9.9 | −9.0 |
| $E_{\pi\perp}$ (M→C:)/$E_{orb}$ | 0.19 | 0.20 | 0.11 | 0.11 | 0.09 | 0.17 | 0.08 | 0.19 | 0.08 | 0.10 | 0.08 | 0.10 | 0.09 |
| $E_{\pi\|\|}$ (M→C:) | −5.7 | −5.4 | −3.8 | −4.1<br>−2.2[a] | −4.4 | −5.7 | −2.5<br>−2.8<br>−4.2[a] | −5.5 | −3.5<br>−4.0[a] | −4.1 | −3.2 | −4.1<br>−2.4[a] | −3.4 |
| E π(C=C)→ π*(C≡O) | − | −1.5 | −3.3 | −4.3 | −3.7 | − | -4.1 | −1.5 | −4.6 | −3.2 | −5.1 | −4.2 | −5.0 |

[a] additional NOCV channels responsible for metal-NHC π-backbonding, which can not be reliably attributed to the orthogonal π⊥ or parallel π|| components

**Comparison of metal-carbon bonding between model σ-complexes $Cp(CO)_2Fe-R$ (7-9) and Fe(II) carbene complexes.** Since transition metal NHDC complexes can be drawn as two resonance forms (Scheme S1 (left), both representations are equally used in literature), in which ditopic ligand formally belongs to anionic $L_2$ and neutral LX-type system, we decided to compare the nature of Fe−carbene bonds in *d*IMes complexes **3** and **5**$^+$ with classic iron-carbon σ-bond in model complexes **7-9** (Scheme S1, right). The optimized geometries of the later species calculated at G09/BP86-D3/Def2-TZVP level are presented in Figure S19. The Fe−C bond distances in both σ-imidazolyl derivatives (**7**: 1.977 Å; **8**: 1.984 Å) are very close to those of Fe−NHC and Fe−*a*NHC bonds in complexes **3** and [**4-6**]$^+$, whereas this bond is rather longer in case of σ-methyl complex **9** (2.068 Å). The AIM analysis of metal-carbon bonding (Table S9) in **7-9** revealed virtually the same metal-carbon bond orders as found in the corresponding NHC derivatives. However, the values of Laplacian $\nabla^2(\rho_c)$ for Fe−C bonds gradually decrease in the row Fe−NHC → Fe−*a*NHC → Fe−heteroaryl → Fe−alkyl (Table S9) being consistent with the increase of ionic bond character from left to right.

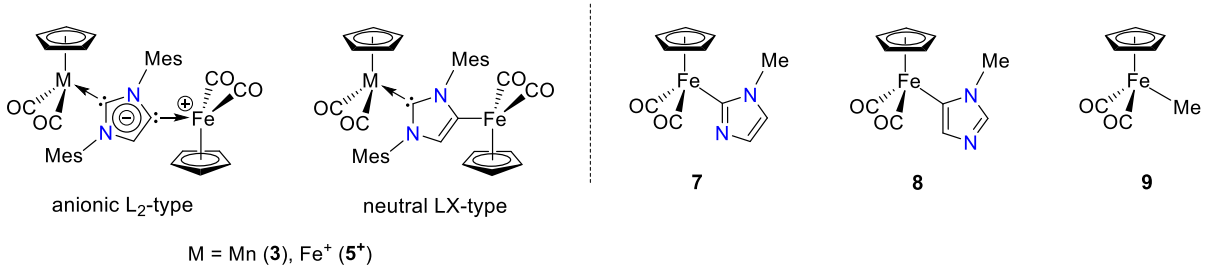


**Scheme S1.** Two possible resonance forms for transition metal NHDC complexes (left) and model σ-complexes $Cp(CO)_2Fe-R$ (**7-9**, right) used for the comparative theoretical investigation of Fe−C4 bonding.

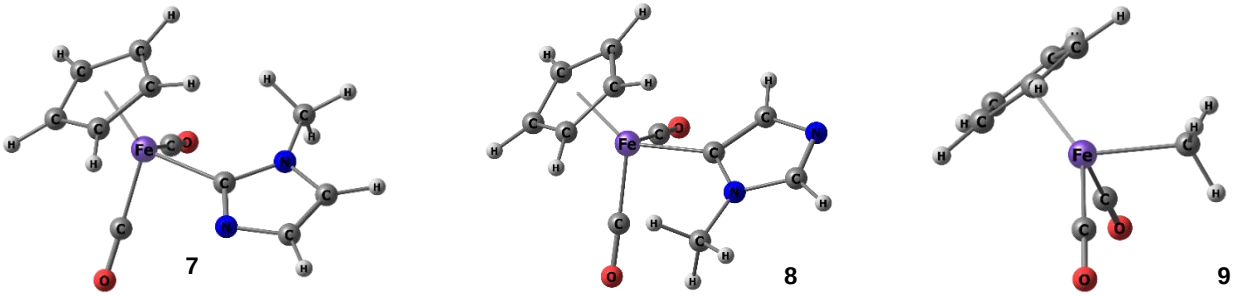


**Figure S19.** DFT optimized geometries for Fe(II) complexes **7** (left), **8** (center) and **9** (right) calculated at G09/BP86-D3/def2-TZVP level.

**Table S9.** Comparison of the selected characteristics of BCPs for Fe−C bonds in optimized Fe(II) σ-complexes **7-9** with those of Fe−NHC bonds in IMes, aIMes and *d*IMes complexes (G09/BP86-D3/Def2-TZVP).[a]

| Complex | **6a**$^+$ NHC | **6b**$^+$ NHC | **4**$^+$ *a*NHC | **3a** *a*NHC | **3b** *a*NHC | **5a**$^+$ NHC | **5a**$^+$ *a*NHC | **5b**$^+$ NHC | **5b**$^+$ *a*NHC | **7** | **8** | **9** |
|---|---|---|---|---|---|---|---|---|---|---|---|---|
| $\rho_c$ | 0.111 | 0.109 | 0.114 | 0.112 | 0.111 | 0.110 | 0.112 | 0.106 | 0.111 | 0.115 | 0.112 | 0.095 |
| $\nabla^2(\rho_c)$ | 0.238 | 0.243 | 0.215 | 0.168 | 0.168 | 0.222 | 0.196 | 0.227 | 0.195 | 0.152 | 0.146 | 0.091 |
| $\varepsilon_c$ | 0.022 | 0.056 | 0.065 | 0.057 | 0.081 | 0.024 | 0.066 | 0.056 | 0.082 | 0.042 | 0.014 | 0.027 |
| $V_c$ | −0.144 | −0.141 | −0.145 | −0.133 | −0.131 | −0.139 | −0.138 | −0.135 | −0.137 | −0.135 | −0.130 | −0.092 |
| $G_c$ | 0.102 | 0.101 | 0.099 | 0.088 | 0.087 | 0.097 | 0.094 | 0.096 | 0.093 | 0.086 | 0.083 | 0.057 |
| $K_c$ | 0.042 | 0.040 | 0.045 | 0.046 | 0.045 | 0.042 | 0.045 | 0.039 | 0.044 | 0.048 | 0.047 | 0.035 |
| $L_c$ | −0.060 | −0.061 | −0.054 | −0.042 | −0.042 | −0.055 | −0.049 | −0.057 | −0.049 | −0.038 | −0.036 | −0.023 |
| DI | 0.782 | 0.779 | 0.799 | 0.791 | 0.787 | 0.776 | 0.792 | 0.769 | 0.789 | 0.781 | 0.795 | 0.793 |

[a] $\rho_c$ – electron density at BCP, a.u.; ε – bond ellipticity; $\nabla^2(\rho_c)$ - Laplacian of Rho = trace of hessian of Rho; V = virial field = potential energy density = trace of stress tensor; G = Lagrangian form of kinetic energy density; K = Hamiltonian form of kinetic energy density = L = K − G = Lagrangian density = (−1/4) $\nabla^2(\rho_c)$; DI = delocalization index = bond order.

Analysis of complexes **7** and **8** using EDA method at ADF/BP86-D3/TZP calculations level (Table S10) revealed that total interaction energies $E_{int}$ of Fe−C bonds are not sensitive to the position of heterocyclic ring in a sharp contrast to those in NHC and *a*NHC derivatives. The values of $E_{int}$ in σ-imidazolyl complexes are 70-90% greater than those found for Fe−NHC and Fe−*a*NHC bonds in cationic species [**4-6**]$^+$. This effect is much less pronounced for Fe−*a*NHC bond in a globally neutral *d*IMes complex **3**, but still remains significant (10-12%). The overall Fe−C bond energy in σ-methyl complex **9** is *ca.* 10% greater than for the corresponding σ-imidazolyl species **8** and **9**. The largest portion of this difference comes from the increase of the electrostatic attraction and repulsion interactions (Table S10). This situation can be more conveniently illustrated by comparing the $E_{steric}$ energy contribution in Fe-carbene bonds being mostly close to zero (0.2 to −5.6 kcal mol$^{-1}$) with highly negative values found in the model σ-complexes **7-9** (−80.5 to −98.3 kcal mol$^{-1}$). The values of $\Delta E_{steric}$ between Fe−*a*NHC bonds in complexes **3a** and **3b** and Fe−C bonds in σ-imidazolyl species **7-8** (23.9-28.3 kcal mol$^{-1}$) is more significant than between the later and σ-methyl complex **9** (14.3-17.8 kcal mol$^{-1}$). In addition, ETS-NOCV analysis data show the increased contribution of σ-donation component in orbital energy of Fe−C interaction described by $E_\sigma/E_{orb}$ ratio going from 0.60-0.63 and 0.68-0.69 for Fe−NHC and Fe−*a*NHC bonds, respectively, to 0.74-75 for Fe−C bond in σ-heteroaryl complexes. Similar trend in $E_\sigma/E_{orb}$ ratio (0.74-0.75 vs. 0.81) was also noticed between Fe(II) σ-imidazolyl (**7** and **8**) and σ-methyl (**9**) complexes. These results show that the Fe−*a*NHC interaction in *d*IMes complexes **3** and **5**$^+$ can be better described as dative bond, which differs significantly from mainly electrostatically-driven Fe−C bonds with pronounced σ-character in model complexes **7-9**. Though according to these data we can not completely rule out partial contribution of LX resonance form (Scheme S1) in complex **3**, our study clearly demonstrates that the most chemically reasonable representation of NHDC complexes includes dicarbene structure with delocalized negative charge within the heterocyclic core.

**Table S10**. The comparison of ETS-NOCV data for Fe−C bonding in optimized Fe(II) σ-complexes **7-9** with those of Fe−NHC bonding in IMes, *a*IMes and *d*IMes complexes (ADF-BP86-D3-TZP, energies are given in kcal mol$^{-1}$).

| Complex | **6a**$^+$ | **6b**$^+$ | **4**$^+$ | **3a** M−*a*NHC | **3b** M−*a*NHC | **5a**$^+$ M−NHC | **5a**$^+$ M−*a*NHC | **5b**$^+$ M−NHC | **5b**$^+$ M−*a*NHC | **7** | **8** | **9** |
|---|---|---|---|---|---|---|---|---|---|---|---|---|
| $E_{Pauli}$ | 144.1 | 145.1 | 155.3 | 172.7 | 173.0 | 141.7 | 150.5 | 145.5 | 149.9 | 194.9 | 194.7 | 195.2 |
| $E_{elst}$ | −145.3 | −144.9 | −160.9 | −229.3 | −228.7 | −145.6 | −154.8 | −146.5 | −153.2 | −278.9 | −275.2 | −293.5 |
| $E_{disp}$ | −23.8 | −24.1 | −16.0 | −17.4 | −17.4 | −24.7 | −17.2 | −24.9 | −17.4 | −9.8 | −10.1 | −5.7 |
| $E_{int}$ | −112.7 | −113.1 | −117.5 | −188.9 | −188.6 | −120.1 | −125.2 | −120.3 | −124.6 | −212.4 | −207.7 | −231.1 |
| $E_{orb}$ | −87.8 | −89.2 | −95.9 | −114.9 | −115.4 | −91.6 | −103.6 | −94.4 | −103.8 | −118.7 | −117.1 | −127.0 |
| $E_{steric} = E_{Pauli} + E_{elst}$ | −1.2 | 0.2 | −5.6 | −56.6 | −55.7 | −3.9 | −4.3 | −1.0 | −3.3 | −84.0 | −80.5 | −98.3 |
| $E_{orb}/E_{int}$ | 0.78 | 0.79 | 0.82 | 0.61 | 0.61 | 0.76 | 0.83 | 0.78 | 0.83 | 0.56 | 0.56 | 0.55 |
| $E_{elstat}/E_{int}$ | 1.29 | 1.28 | 1.37 | 1.21 | 1.21 | 1.21 | 1.24 | 1.22 | 1.23 | 1.31 | 1.32 | 1.37 |
| $E_\sigma$ (C→M) | −54.3 | −53.9 | −64.8 | −78.2 | −77.9 | −57.3 | −71.5 | −57.5 | −71.3 | −87.6 | −87.7 | −103.3 |
| $E_\sigma$ (C→M)/$E_{orb}$ | 0.62 | 0.60 | 0.68 | 0.68 | 0.68 | 0.63 | 0.69 | 0.61 | 0.69 | 0.74 | 0.75 | 0.81 |
| $E_{\pi\perp}$ (M→C) | −9.6 | −9.8 | −9.1 | −8.7 | −8.9 | −9.2 | −8.7 | −9.9 | −9.0 | −8.1 | −7.9 | −4.1[b] |
| $E_{\pi\perp}$ (M→C)/$E_{orb}$ | 0.11 | 0.11 | 0.09 | 0.08 | 0.08 | 0.10 | 0.08 | 0.10 | 0.09 | 0.07 | 0.07 | 0.03 |
| $E_\pi$ (M→C)[a] | −3.8 | −6.3 | −4.4 | −9.5[j] | −7.5 | −4.1 | −3.2 | −6.5 | −3.4 | −7.3 | −6.9 | −3.1[b] |

[a] The sum of energies for other π interactions. [b] The interaction energy corresponding to the overlap between metal orbitals and σ*-orbitals of C−H bonds in the methyl group.

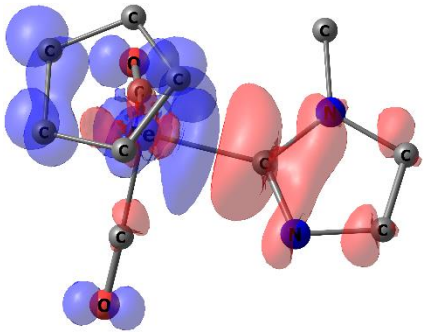

**NOCV1**, E = –87.6 (σC→M)

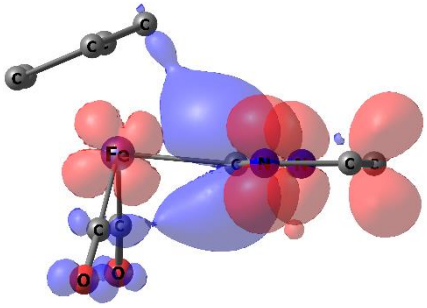

**NOCV2**, E = –8.1 (π1 M→C)

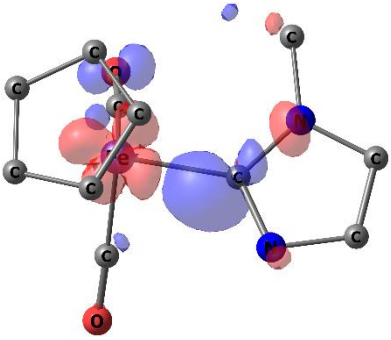

**NOCV3**, E = –4.6 (π2 M→C)

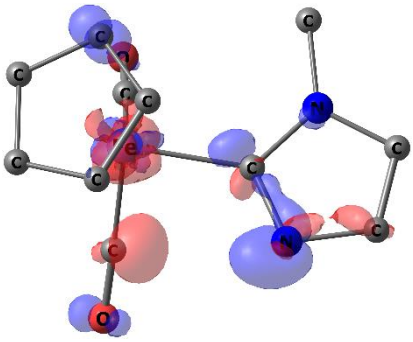

**NOCV4**, E = –2.3 (other M→C)

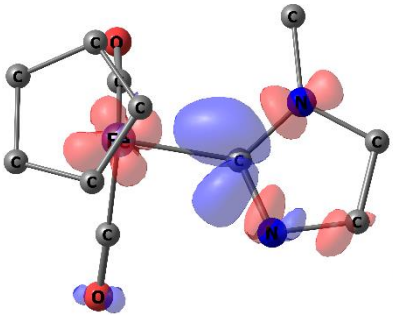

**NOCV5**, E = –2.7 (π2 M→C)

**Figure S20.** NOCV deformation electron density for complex **7** (isosurface at 0.003 and 0.001 a.u. for NOCV1 and NOCV2-5, respectively) and associated energies in kcal mol$^{-1}$. Red areas correspond to the depletion and blue to the concentration of electron density. Hydrogen atoms are omitted for clarity.

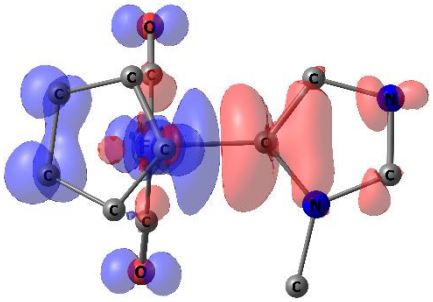

**NOCV1**, E = –87.7 (σC→M)

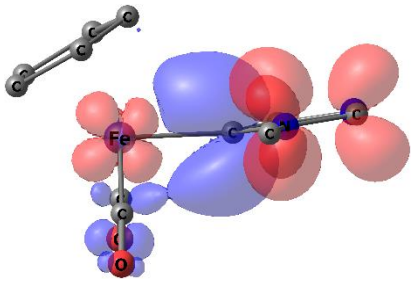

**NOCV2**, E = –7.9 (π1 M→C)

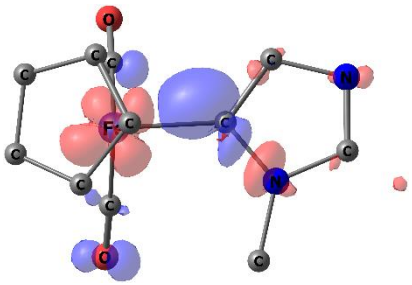

**NOCV3**, E = –4.1 (π2 M→C)

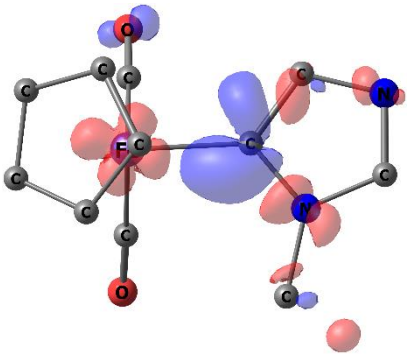

**NOCV4**, E = –2.8 (π2 M→C)

**Figure S21.** NOCV deformation electron density for complex **8** (isosurface at 0.003 and 0.001 a.u. for NOCV1 and NOCV2-4, respectively) and associated energies in kcal mol$^{-1}$. Red areas correspond to the depletion and blue to the concentration of electron density. Hydrogen atoms are omitted for clarity.

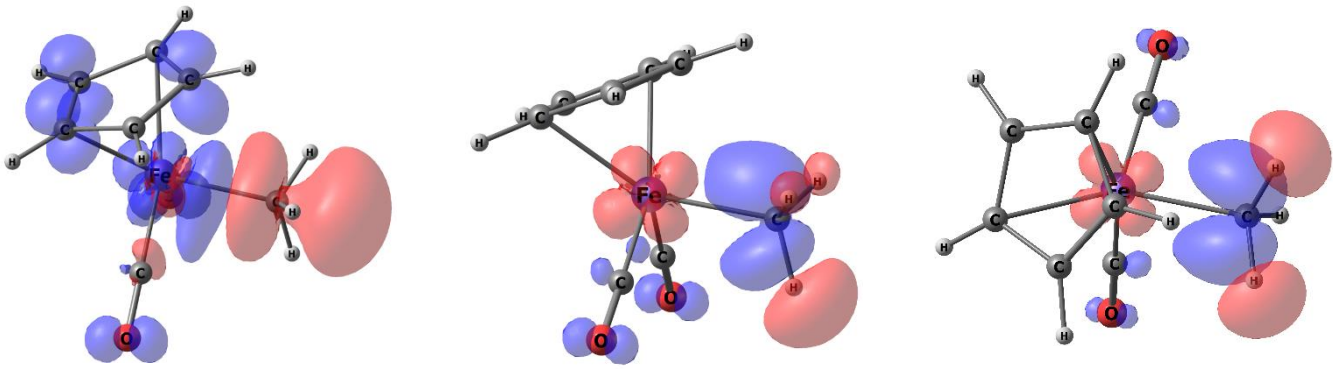

**NOCV1**, E = –103.3 (σC→M) **NOCV2**, E = –4.1 (π1 M→C−H) **NOCV3**, E = –3.1 (π2 M→C−H)

**Figure S22.** NOCV deformation electron density for complex **9** (isosurface at 0.003 and 0.001 a.u. for NOCV1 and NOCV2-3, respectively) and associated energies in kcal $mol^{-1}$. Red areas correspond to the depletion and blue to the concentration of electron density.

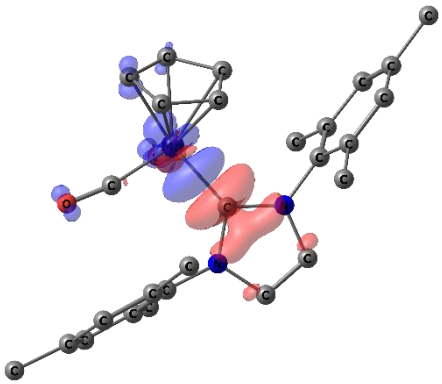

**NOCV1**, E = –38.8 (σC:→M)

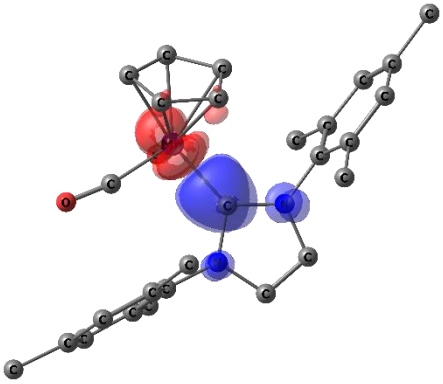

**NOCV2**, E = –13.9 ($\pi_{\perp}$ M→C:)

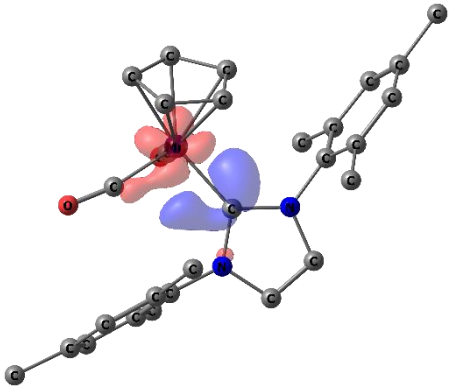

**NOCV3**, E = –5.4 ($\pi_{||}$ M→C:)

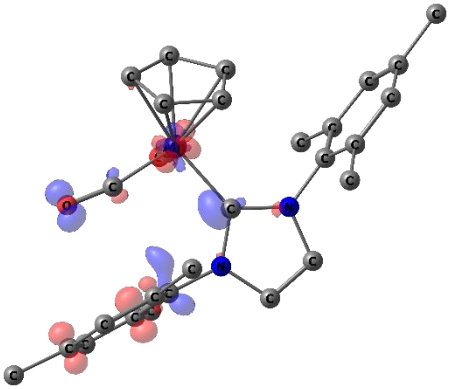

**NOCV4**, E = –1.5 (π(C=C)→π*(CO))

**Figure S23.** NOCV deformation electron density for complex **1b** (isosurface at 0.003 and 0.001 a.u. for NOCV1 and NOCV2-4, respectively) and associated energies in kcal $mol^{-1}$. Red areas correspond to the depletion and blue to the concentration of electron density. Hydrogen atoms are omitted for clarity.

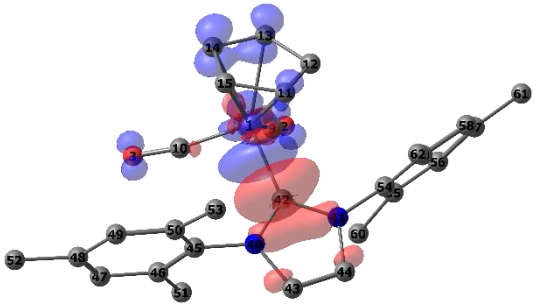

**NOCV1**, E = –54.3 (σC:→M)

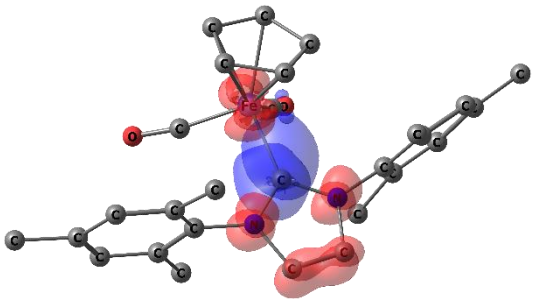

**NOCV2**, E = –9.6 ($\pi_{\perp}$ M→C:)

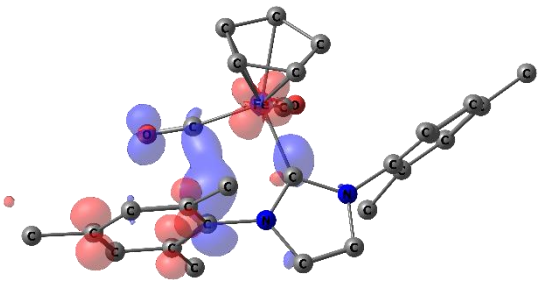

**NOCV3**, E = –3.3 (π(C=C)→π*(CO))

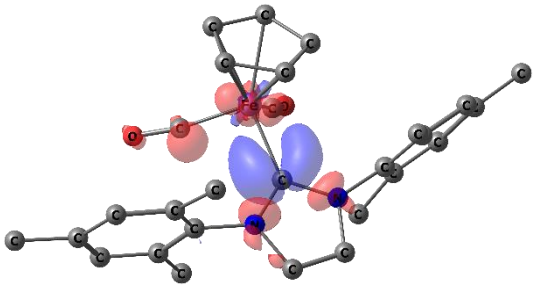

**NOCV4**, E = –3.8 ($\pi_{||}$ M→C:)

**Figure S24.** NOCV deformation electron density for complex **6a**$^{+}$ (isosurface at 0.003 and 0.001 a.u. for NOCV1 and NOCV2-4, respectively) and associated energies in kcal $mol^{-1}$. Red areas correspond to the depletion and blue to the concentration of electron density. Hydrogen atoms are omitted for clarity.

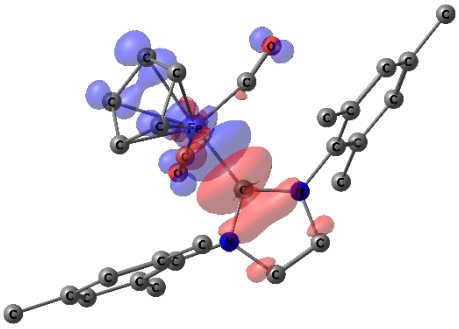

**NOCV1**, E = –53.9 (σC:→M)

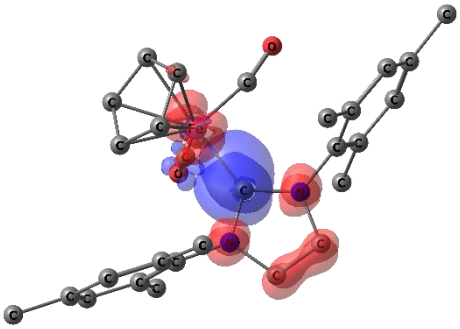

**NOCV2**, E = –9.8 ($\pi_{\perp}$ M→C:)

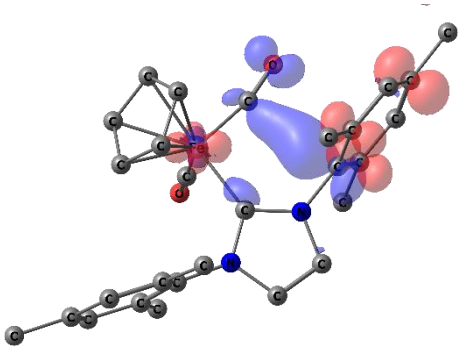

**NOCV3**, E = –4.3 (π(C=C)→π*(CO))

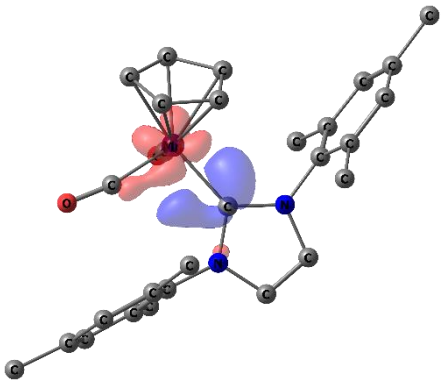

**NOCV4**, E = –4.1 ($\pi_{||}$ M→C:)

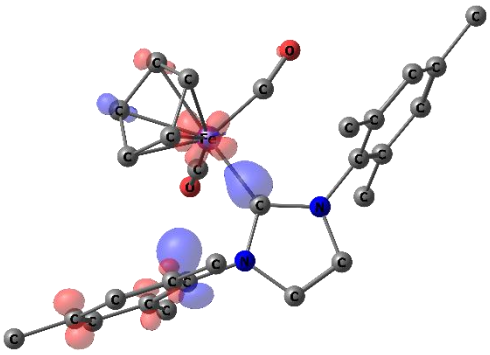

**NOCV5**, E = –2.2 (π M→C:)

**Figure S25.** NOCV deformation electron density for complex **6b**$^{+}$ (isosurface at 0.003 and 0.001 a.u. for NOCV1 and NOCV2-5, respectively) and associated energies in kcal mol$^{-1}$. Red areas correspond to the depletion and blue to the concentration of electron density. Hydrogen atoms are omitted for clarity.

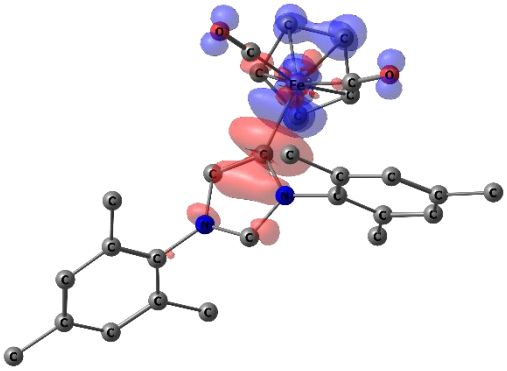

**NOCV1**, E = –64.8 (σC:→M)

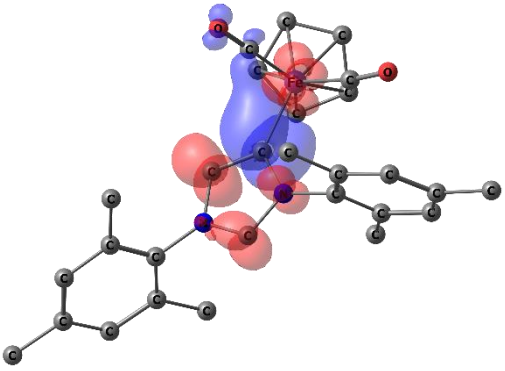

**NOCV2**, E = –9.1 ($\pi_{\perp}$ M→C:)

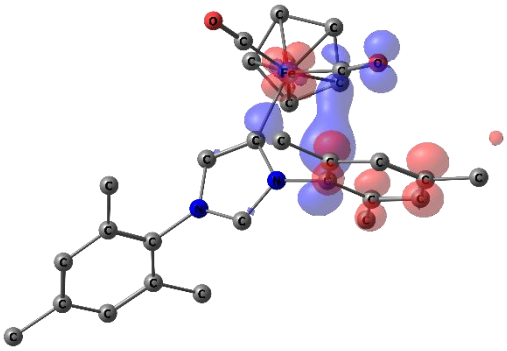

**NOCV3**, E = –3.7 (π(C=C)→π*(CO))

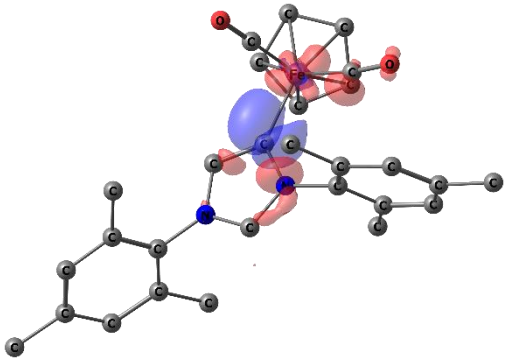

**NOCV4**, E = –4.4 ($\pi_{||}$ M→C:)

**Figure S26.** NOCV deformation electron density for complex $\mathbf{4}^{+}$ (isosurface at 0.003 and 0.001 a.u. for NOCV1 and NOCV2-4, respectively) and associated energies in kcal $mol^{-1}$. Red areas correspond to the depletion and blue to the concentration of electron density. Hydrogen atoms are omitted for clarity.

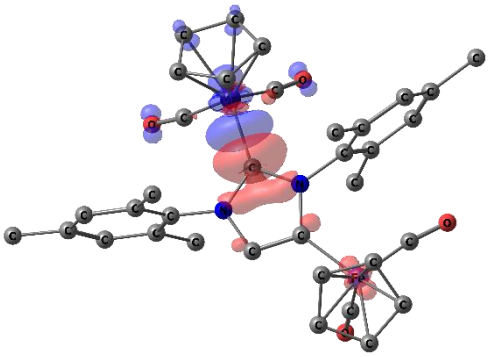

**NOCV1**, E = –38.6 (σC:→M)

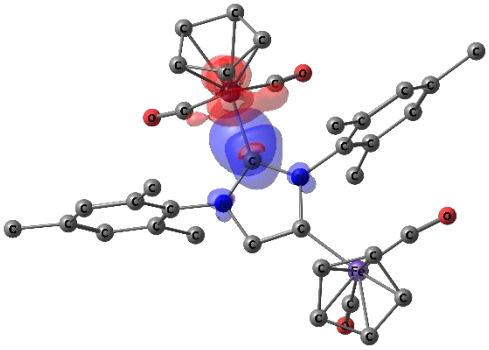

**NOCV2**, E = –11.2 ($\pi_{\perp}$ M→C:)

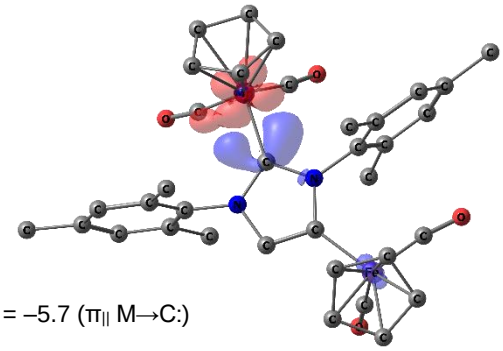

**NOCV3**, E = –5.7 ($\pi_{||}$ M→C:)

**Figure S27.** NOCV deformation electron density for Mn−NHC bond in complex **3a** (isosurface at 0.003 and 0.001 a.u. for NOCV1 and NOCV2-3, respectively) and associated energies in kcal $mol^{-1}$. Red areas correspond to the depletion and blue to the concentration of electron density. Hydrogen atoms of aryls are omitted for clarity.

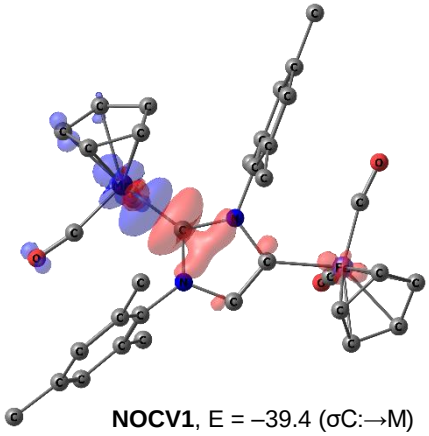

**NOCV1**, E = –39.4 (σC:→M)

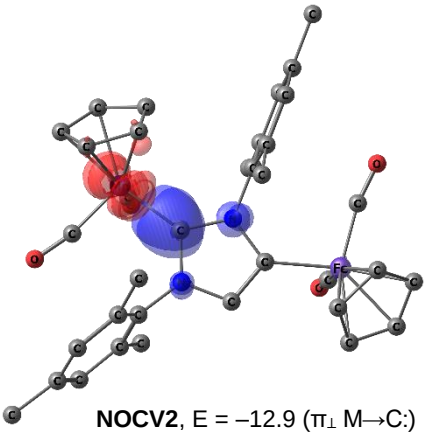

**NOCV2**, E = –12.9 ($\pi_{\perp}$ M→C:)

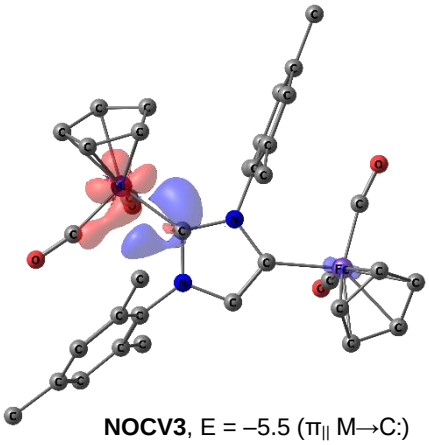

**NOCV3**, E = –5.5 ($\pi_{||}$ M→C:)

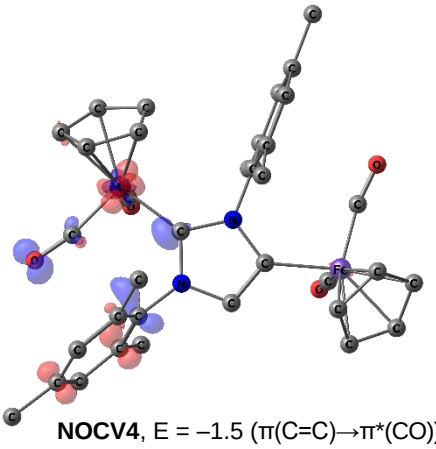

**NOCV4**, E = –1.5 (π(C=C)→π*(CO))

**Figure S28.** NOCV deformation electron density for Mn−NHC bond in complex **3b** (isosurface at 0.003 and 0.001 a.u. for NOCV1 and NOCV2-4, respectively) and associated energies in kcal.$mol^{-1}$. Red areas correspond to the depletion and blue to the concentration of electron density. Hydrogen atoms of aryls are omitted for clarity.

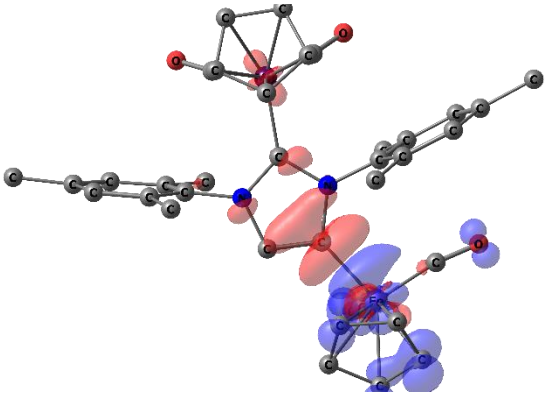

**NOCV1**, E = –78.2 (σC:→M)

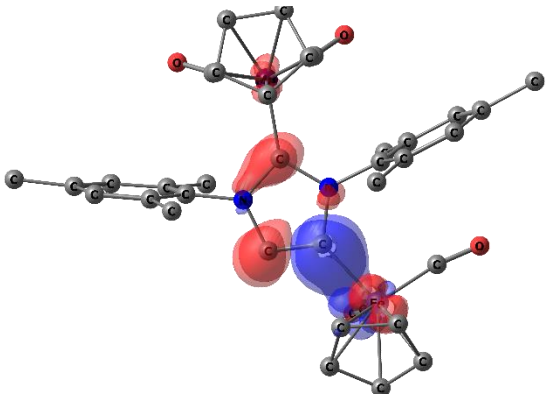

**NOCV2**, E = –8.7 ($\pi_{\perp}$ M→C:)

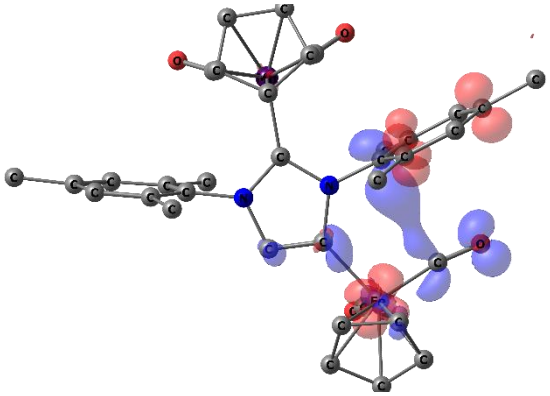

**NOCV3**, E = –4.1 (π(C=C)→ π*(CO))

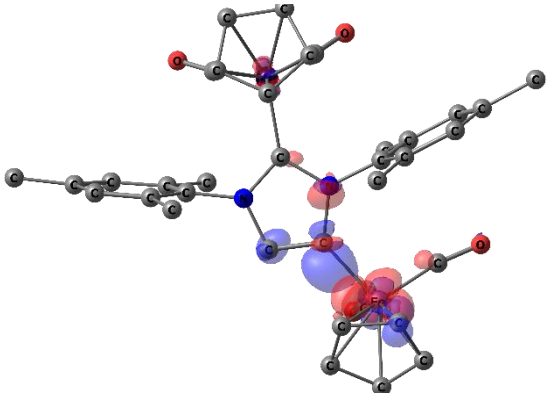

**NOCV4**, E = –4.2 (π M→C:)

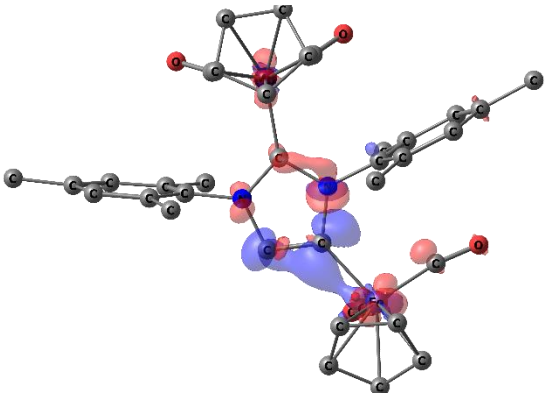

**NOCV5**, E = –2.8 ($\pi 1_{||}$ M→C:)

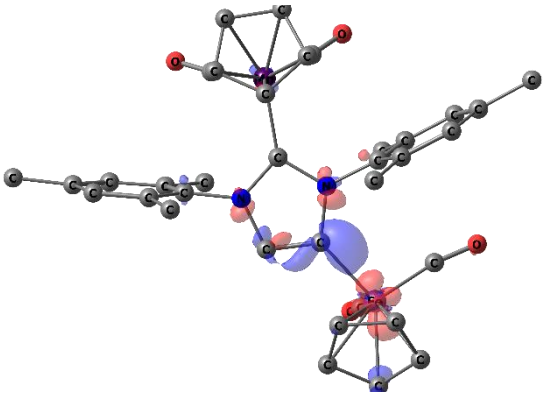

**NOCV6**, E = –2.5 ($\pi 2_{||}$ M→C:)

**Figure S29.** NOCV deformation electron density for Fe−*a*NHC bond in complex **3a** (isosurface at 0.003 and 0.001 a.u. for NOCV1 and NOCV2-6, respectively) and associated energies in kcal $mol^{-1}$. Red areas correspond to the depletion and blue to the concentration of electron density. Hydrogen atoms of aryls are omitted for clarity.

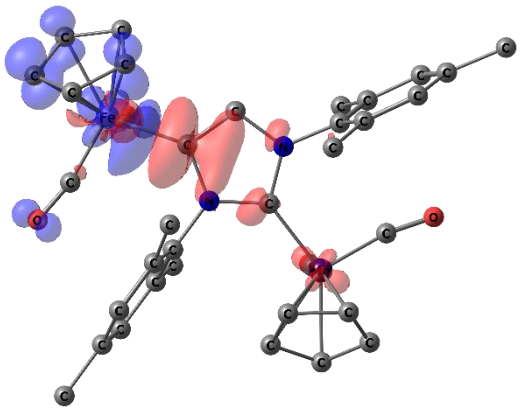

**NOCV1**, E = –77.9 (σC:→M)

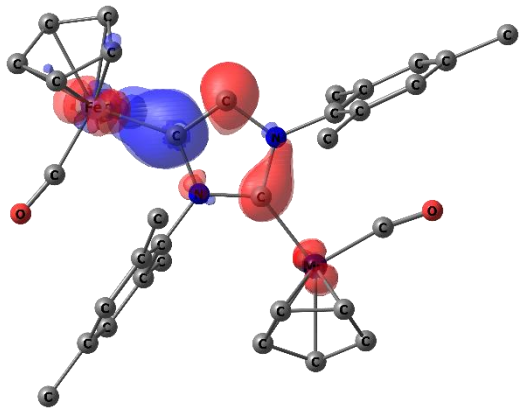

**NOCV2**, E = –8.9 ($\pi_{\perp}$ M→C:)

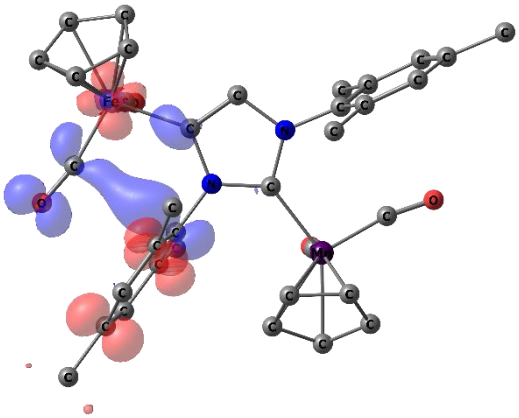

**NOCV3**, E = –4.6 (π(C=C)→π*(CO))

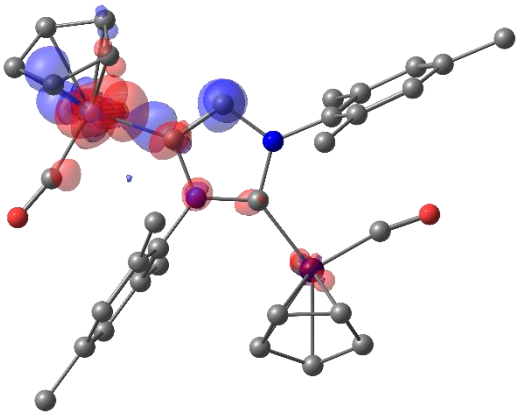

**NOCV4**, E = –4.0 (π M→C:)

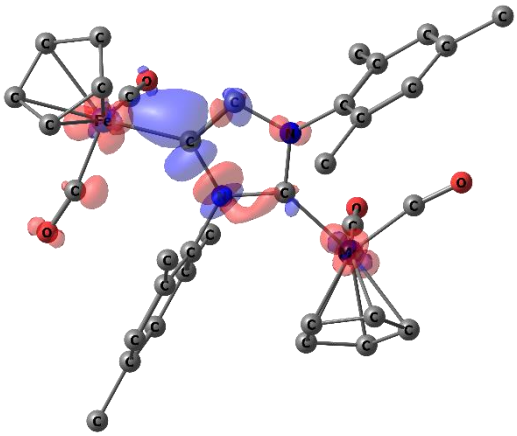

**NOCV5**, E = –3.5 ($\pi_{||}$ M→C:)

**Figure S30.** NOCV deformation electron density for Fe−*a*NHC bond in complex **3b** (isosurface at 0.003 and 0.001 a.u. for NOCV1 and NOCV2-5, respectively) and associated energies in kcal $mol^{-1}$. Red areas correspond to the depletion and blue to the concentration of electron density. Hydrogen atoms of aryls are omitted for clarity.

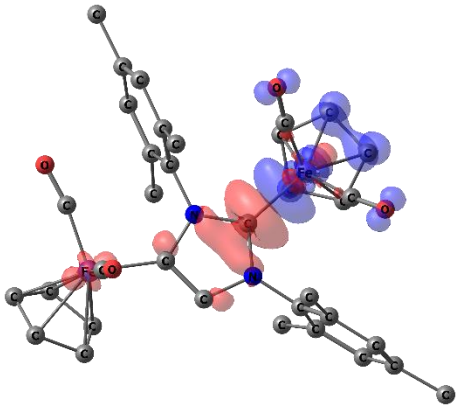

**NOCV1**, E = –57.3 (σC:→M)

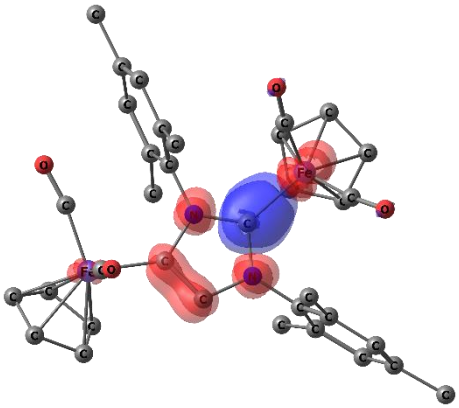

**NOCV2**, E = –9.2 ($\pi_{\perp}$ M→C:)

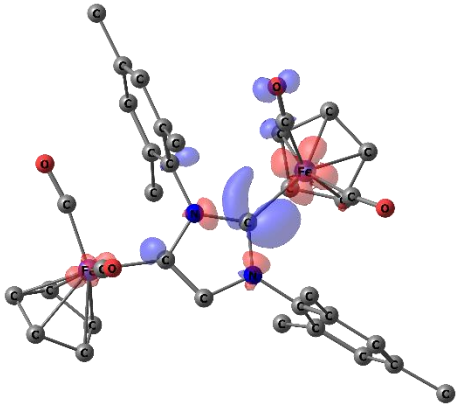

**NOCV3**, E = –4.1 ($\pi_{||}$ M→C:)

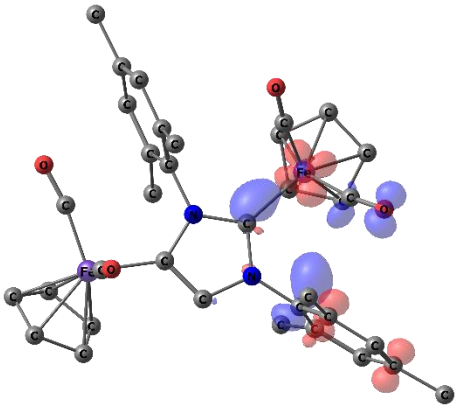

**NOCV4**, E = –3.2 (π(C=C)→π*(CO))

**Figure S31.** NOCV deformation electron density for Fe−NHC bond in complex **5a**$^{+}$ (isosurface at 0.003 and 0.001 a.u. for NOCV1 and NOCV2-4, respectively) and associated energies in kcal mol$^{-1}$. Red areas correspond to the depletion and blue to the concentration of electron density. Hydrogen atoms of aryls are omitted for clarity.

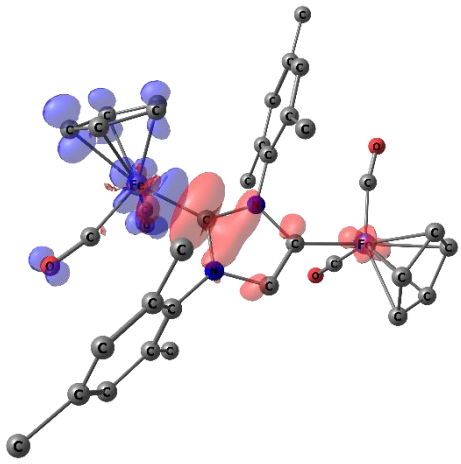

**NOCV1**, E = –57.5 (σC:→M)

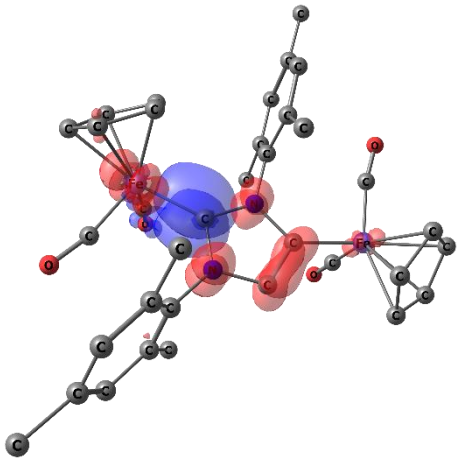

**NOCV2**, E = –9.9 ($\pi_{\perp}$ M→C:)

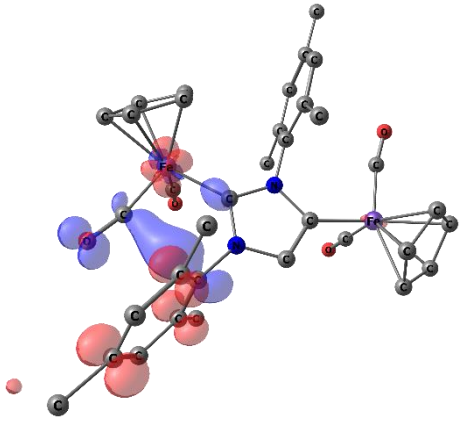

**NOCV3**, E = –4.2 (π(C=C)→π*(CO))

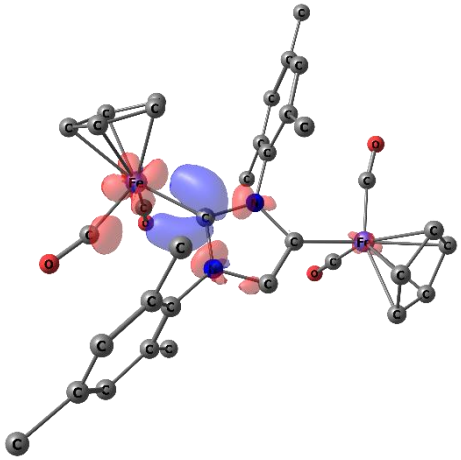

**NOCV4**, E = –4.1 ($\pi_{||}$ M→C:)

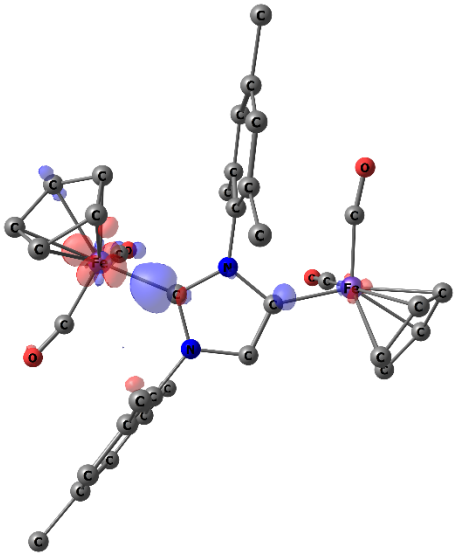

**NOCV5**, E = –2.4 (π M→C:)

**Figure S32.** NOCV deformation electron density for Fe−NHC bond in complex **5b**$^{+}$ (isosurface at 0.003 and 0.001 a.u. for NOCV1 and NOCV2-5, respectively) and associated energies in kcal mol$^{-1}$. Red areas correspond to the depletion and blue to the concentration of electron density. Hydrogen atoms of aryls are omitted for clarity.

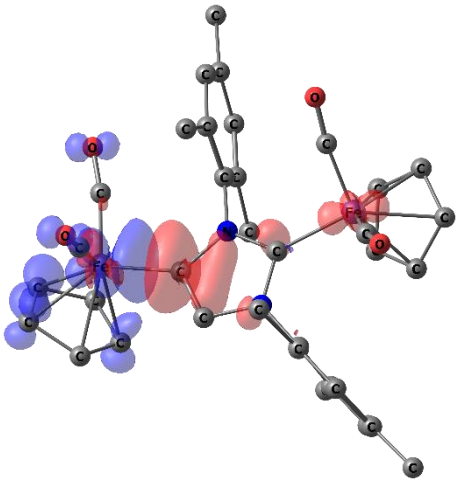

**NOCV1**, E = –71.5 (σC:→M)

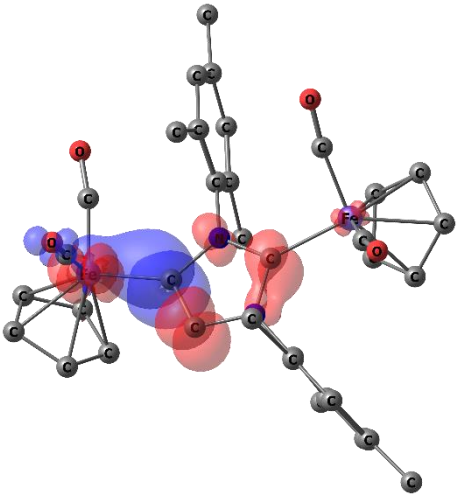

**NOCV2**, E = –8.7 ($\pi_{\perp}$ M→C:)

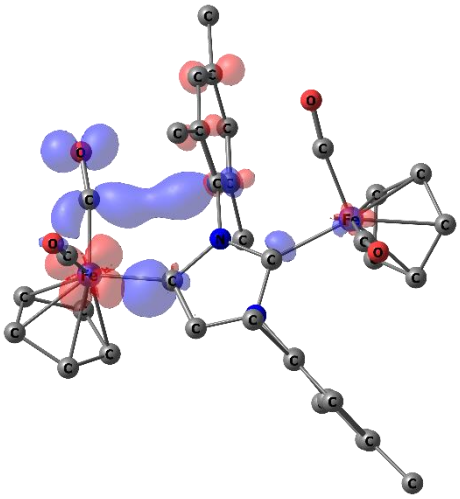

**NOCV3**, E = –5.1 (π(C=C)→π*(CO))

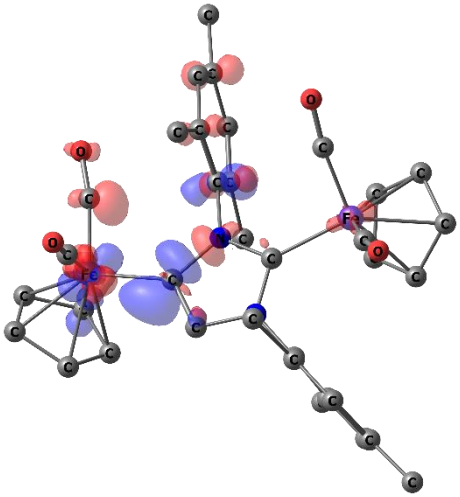

**NOCV4**, E = –3.2 ($\pi_{||}$ M→C:)

**Figure S33.** NOCV deformation electron density for Fe−*a*NHC bond in complex **5a**$^{+}$ (isosurface at 0.003 and 0.001 a.u. for NOCV1 and NOCV2-4, respectively) and associated energies in kcal mol$^{-1}$. Red areas correspond to the depletion and blue to the concentration of electron density. Hydrogen atoms of aryls are omitted for clarity.

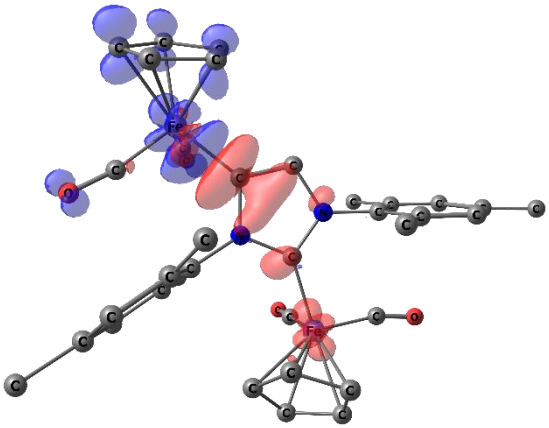

**NOCV1**, E = –71.3 (σC:→M)

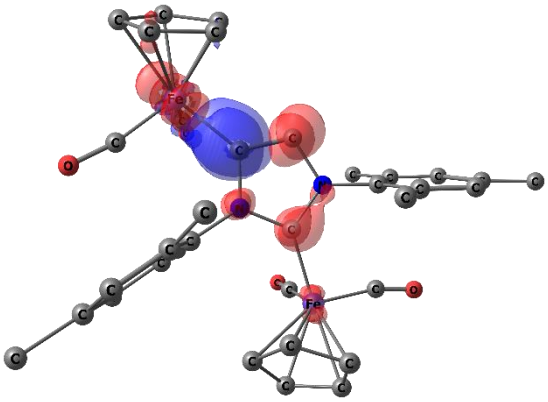

**NOCV2**, E = –9.0 ($\pi_{\perp}$ M→C:)

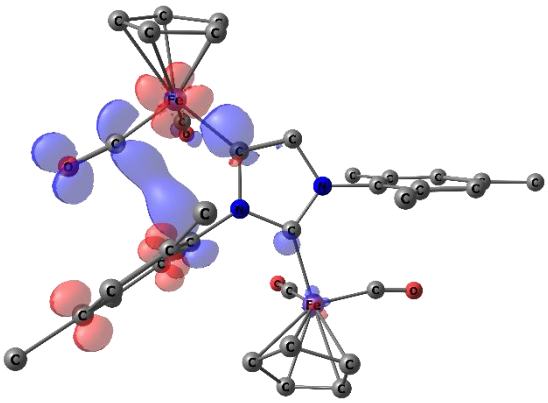

**NOCV3**, E = –5.0 (π(C=C)→π*(CO))

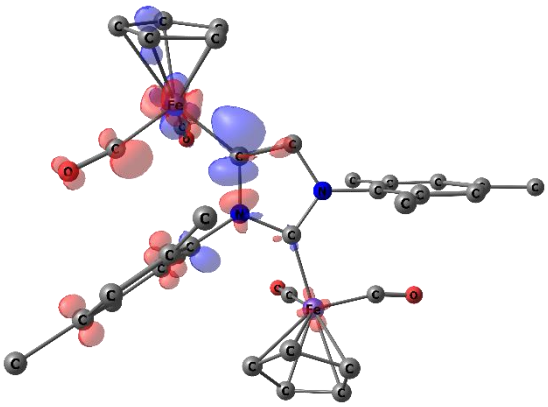

**NOCV4**, E = –3.4 ($\pi_{||}$ M→C:)

**Figure S34.** NOCV deformation electron density for Fe−*a*NHC bond in complex **5b**$^{+}$ (isosurface at 0.003 and 0.001 a.u. for NOCV1 and NOCV2-4, respectively) and associated energies in kcal mol$^{-1}$. Red areas correspond to the depletion and blue to the concentration of electron density. Hydrogen atoms of aryls are omitted for clarity.